2007

Thermal Shock Fracture Behaviors of Functionally Graded Ceramics

Wenjin Luo

THERMAL SHOCK FRACTURE BEHAVIOR OF FUNCTIONALLY GRADED CERAMICS

By

Wenjin Luo

B.S. Beijing Union University, 1987

A THESIS

Submitted in Partial Fulfillment of the

Requirements for the Degree of

Master of Science

(in Mechanical Engineering)

The Graduate School

The University of Maine

December, 2006

Advisory Committee:

Zhihe Jin, Assistant Professor of Mechanical Engineering, Advisor

Michael Peterson Jr., Professor of Mechanical Engineering, Co-advisor

Donald A. Grant, Chair and Professor of Mechanical Engineering

Senthil Vel, Associate Professor of Mechanical Engineering

THERMAL SHOCK FRACTURE BEHAVIOR OF FUNCTIONALLY GRADED CERAMICS

By

Wenjin Luo

Thesis Advisor: Dr. Zhihe Jin

This thesis uses a thermal fracture mechanics model to study the thermal shock fracture behavior of functionally graded ceramics (FGC). The specimen used in this study is a FGC strip with an edge crack on one surface. A severe thermal shock is applied on the cracked surface. The temperature field in a thermally shocked FGC strip is evaluated first using a closed form solution. Thermal stresses, thermal stress intensity factors (TSIF) and critical thermal shocks are evaluated using a thermomechanics and fracture mechanics approach. The effective thermal properties of the FGC specimens are estimated using micromechanics models for conventional composites. Some numerical results of critical thermal shocks are provided for FGC specimens with constant elastic material properties and graded thermal properties in the thickness direction of the strips. Also, examples of thermal stresses and thermal stress intensity factors (TSIFs) are

provided. The results show that the components gradation of the FGC composites has significant influence on the specimens' thermal shock behavior. When the volume fraction of the FGC strip is changed rapidly, the critical thermal shock is changed dramatically.

DEDICATION

Dedicated to my wife Lin Lin

ACKNOWLEGEMENTS

TABLE OF CONTENTS

LIST OF TABLES

LIST OF FIGURES

CHAPTER 1

INTRODUCTION

Ceramic materials are widely used in engineering applications because they have some desirable material properties. Most ceramic materials consist of metal oxides, metal nitrides, metal carbides and others. Ceramics are used to coat the surface of metals or other ceramics subjected to severe usage. Most ceramic coated cutting tools are harder than metal cutting tools; therefore, they may have better performance and a longer life. Ceramic coated cutting tools are used to cut some metals which cannot be cut by using normal cutting procedures because of the potential of a chemical reaction between the two materials. Another important application of ceramics is to coat turbine engine blades because of ceramic's outstanding high temperature and corrosion resistance (Pettit and Goward, 1983).

Despite the advantages, ceramics suffer from certain disadvantages which limit their usage in many engineering applications. Most ceramic materials have low toughness because of inherent brittleness and micro cracks. The sharp interface between ceramic coatings and base materials may induce a huge stress concentration when the ceramic coated parts are under load. This stress concentration may cause catastrophic material failure. To overcome these disadvantages, functionally graded ceramics (FGC) were recently introduced.

An FGC is a ceramic or ceramic-ceramic composite with a gradually changing microstructure and macro material properties (Koizumi, 1993). FGCs have higher performance than conventional ceramic composites because of the gradual variation in volume fractions of the constituent materials which have different material properties. These characteristics eliminate the sharp interface between components and thus reduce their stress concentration. Functional grading also enhances the bonding strength between dissimilar components. Compared to conventional ceramic composites, FGCs perform better under severe environmental attacks and have higher strength and fracture toughness. In a study Hasselman and Youngblood (Hasselman and Youngblood, 1978) showed a much smaller tensile thermal stress in the FGC ceramic cylinder than in a homogeneous one. Under thermal shock, FGC coatings have significantly less damage than conventional ceramic coatings (Kuroda et al. 1993).

High temperature applications are among the most important engineering fields where ceramics are used. Knowing the thermal fracture behavior of FGCs is critical for material design and improvement. Temperature gradients exist in FGCs, which may induce thermal stresses and cause material failure. FGC strips can be used to model very important engineering applications. Most of the strips have graded material properties only in the thickness direction. Under thermal load, the temperature distribution varies in the thickness direction when the load is applied on the surfaces. Ishiguro et al. (Ishiguro et al., 1993) studied the one-dimensional temperature profile in a strip of functionally graded material (FGM) using a multi-layered material model. Obata and Noda (Obata and Noda, 1993a, 1993b) probed 1-D heat conduction in a FGM plate using perturbation

techniques. Tanigawa et al. (Tanigawa et al., 1996) provided a one-dimensional temperature distribution in a FGM plate using a laminated composite with homogeneous layers. Jin and Paulino (Jin and Paulino, 2001) studied short time temperature distribution in a FGM strip using the layered material model. Jin (Jin, 2002) obtained a simple closed-form short time 1-D asymptotic temperature solution using a multi-layered material model and asymptotic technique. Qian and Batra (Qian and Batra, 2005) studied three-dimensional heat conduction in a thick FGM plate by using a higher-order plate theory and a meshless local Petrov-Galerkin (MLPG) method.

The temperature gradient in FGMs may cause thermal stress distributions. Kawasaki and Watanabe (Kawasaki and Watanabe, 1987) analyzed the thermal stress of a FGC composite using a finite element method. Satyamurthy and co-workers (Satyamurthy et al., 1990) studied the effect of the spatial variation of thermal conductivity on the magnitude of tensile thermal stress field in brittle materials under a convective thermal load. The studies showed that spatial variation of thermal conductivities of the FGMs reduced the thermal stresses significantly. Arai et al. (Arai et al, 1991) analyzed the elastic-plastic thermal stress in FGM for the purpose of optimum design. Noda and Tsuji (Noda and Tsuji, 1991a and 1991b) studied the thermal stress field in the FGM composites. Vel and Batra (Vel and Batra, 2002) obtained an exact solution for three-dimensional deformation of a simply supported thick FGM plate with transient mechanical and thermal loads on its top and/or bottom surfaces. Vel and Batra (Vel and Batra, 2003) also presented an analytical solution for three-dimensional

thermoplastic deformations of a simply supported rectangular FGM plate under a time-dependent thermal load on the top and /or bottom surfaces.

In studying the thermal fracture behavior of FGMs, thermal stress intensity factors (TSIFs) are used to predict their fracture behaviors and optimize the designs of the FGM composites when a crack presents. Jin and Noda (Jin and Noda, 1993) and Noda and Jin (Noda and Jin, 1993) considered steady state thermal fracture of FGMs. Kawasaki and Watanabe (Kawasaki and Watanabe, 1993a, 1993b) studied the fabrication of disk-shaped FGM by hot pressing and the thermal shock fracture mechanisms of FGMs with surface cracks subjected to side heating and cooling. Takahashi et al. (Takahashi et al, 1993) probed the thermal shock/fatigue fracture behavior of surface crack in FGMs. Jin and Noda (Jin and Noda, 1994a) investigated crack-tip singular fields in non-homogeneous materials. Jin and Noda (Jin and Noda, 1994b) studied an edge crack in a nonhomogeneous half-plane under thermal loading. Jin and Noda (Jin and Noda, 1994c) investigated TSIFs for a crack in a semi-infinite plane of a FGM. Erdogan and Wu (Erdogan and Wu, 1996) obtained the solution of TSIF for FGMs subjected to steady state thermal load. Jin and Batra (Jin and Batra, 1996b) studied an FGM strip with an edge crack. Tanigawa et al. (Tanigawa et al., 1996) investigated a nonhomogeneous material with a penny-shaped crack. Noda (Noda, 1997) and Fujimoto and Noda (Fujimoto and Noda, 2001a, 2001b) used a finite element method to investigate the crack growth in an FGM plate under transit thermal load. Choi et al. (Choi et al., 1998) probed a layered half-plane with collinear cracks; the plane has a graded homogeneous interfacial zone. Lee and Erdogan (Lee and Erdogan, 1998) studied the thermal stress of

interface cracking in FGM coatings under steady state heat flow. Nemat-Alla and Noda (Nemat-Alla and Noda, 2000) studied a semi-infinite FGC plate with an edge crack when the coefficient of thermal expansion varied in two directions. Wang et al. (Wang et al, 2000) used a laminated material model to study crack problems in FGMs under transit thermal loading condition. Jin and Paulino (Jin and Paulino, 2001) studied an edge cracked FGM strip with constant elastic moduli and graded thermal properties. Ueda (Ueda, 2001, 2002) studied thermal shock fracture in a graded W-Cu divertor plate. Jin (Jin, 2003a) investigated the effect of thermal property gradients on the edge cracking in a FGM coating bonded to a homogeneous substrate subjected to a thermal shock. Pindera et al. (Pindera et al., 2002) used their high-order theory to investigate spallation in thermal barrier coatings. Zhao et al. (Zhao et al., 2002) presented a model for design of FGC tool materials with a symmetrical composition distribution. Huang and co-workers (Huang et al., 2004) developed a new model for fracture analysis of functionally graded materials with arbitrarily varying material properties under thermal load. Rangaraj and Kokini (Rangaraj and Kokini, 2004) used two-dimensional finite element models with a cohesive zone to study quasi-static crack extension in functionally graded yttria stabilized zirconia (YSZ)-Bond Coat (BC) alloy thermal barrier coatings (TBC). Wang et al. (Wang et al., 2004) used a finite element/finite difference (FE/FD) method to study the thermal shock resistance of FGMs and provide the critical thermal shock. Zhao and co-workers (Zhao et al., 2004) studied the thermal shock resistance of Al_2O_3-TiC and Al_2O_3-(W, Ti)C FGC tool materials with symmetrical structures by using finite element/finite difference (FE/FD) method. Kokini and Rangaraj (Kokini and Rangaraj,

2005) studied the thermal fracture and its time-dependent behavior in functionally graded yttria stabilized zirconia-NiCoCrAlY bond coat alloy thermal barrier coatings. Yildirim et al. (Yildirim et al., 2005) calculated TSIF in a three dimensional FGM coating using a correlation technique of a finite element method. Dag (Dag, 2006) developed a new computational method based on the equivalent domain integral (EDI) for mode I fracture analysis to orthotropic FGMs subjected to thermal stresses. El-Borgi et al. (El-Borgi et al., 2006) considered an embedded partially insulated crack in a graded coating bonded to a homogeneous substrate under thermal and mechanical loading. Carpinteri and Pugno (Carpinteri and Pugno, 2006) analyzed the stress field and fracture propagation due to thermal loading in multi-layered and/or functionally graded composite materials. Extensive reviews on thermal stress and fracture in FGM had been done by Tanigawa (Tanigawa, 1995) and Noda (Noda, 1999).

When a thermal shock is applied to a FGC specimen, the pre-existing crack may grow depending on the severity of the thermal load. There is a critical value for the thermal shock called critical thermal shock and it is denoted by ΔT_c. When the applied thermal load is greater than the critical thermal shock, the crack starts to grow; otherwise, the crack remains unchanged. The critical thermal shock indicates how severe of a thermal load can be applied to a specimen without combined crack growth.

In this work, we use an analytical and semi-analytical method to evaluate critical thermal shocks for three FGCs, i.e., Al_2O_3/Si_3N_4, TiC/SiC and TiC/B_4C. The strips have the same geometry as described by Fig. 1.1. We assume that the vertical and horizontal dimension of the strip is much greater than its thickness b. The pre-existing crack is on

one of the thickness surfaces. The strips can be used to model ceramic cutting tools and turbine engine blades in engineering applications.
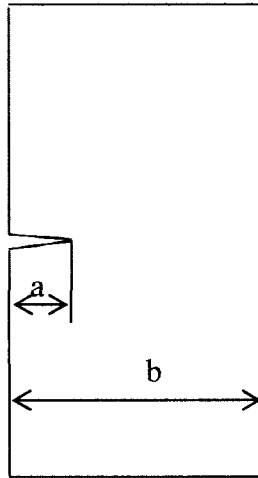
Figure 1.1 The geometry of the FGC strips

To simplify the study, but still keep the generality, we assume that the thermal shock is only applied on the cracked surface of the FGC strips. One dimensional heat conduction equations are used with appropriate boundary conditions to calculate the temperature field. A linear thermal elasticity approach is employed to solve the boundary value problem for the thermal stress distribution. The thermal stress intensity factor (TSIF) is then evaluated by using linear elastic thermal fracture mechanics. Once the TSIF is calculated, it is set to be equal to the fracture toughness of the FGC composite, and then the critical thermal shock is obtained. We assume these FGC strips have constant elastic moduli and various thermal properties in the thickness direction (x direction) following a power law function. These strips can be obtained in reality by

dispersing ceramic particulates in a ceramic matrix with elastic moduli similar to that of the ceramic particulates.

Chapter 2 of this thesis reviews the fracture mechanics of ceramics. Fracture toughnesses for particular ceramic materials are summarized. Chapter 3 reviews thermal stress and thermal shock behavior of ceramics. Basic heat conduction equations in solids and basic thermoelasticity equations are given; temperature field, thermal stress field and critical thermal shock for a ceramic strip are introduced. Chapter 4 reviews basic equations of thermoelasticity of FGCs and the micromechanics models to calculate effective thermal and elastic properties of FGCs. Chapter 5 studies the temperature field using a one-dimensional heat conduction method, the thermal stress field using a linear thermal elasticity method, and thermal stress intensity factor field using linear thermal fracture mechanics for the thermally shocked FGC strips with edge cracks. Numerical results of temperature fields, thermal stress fields and thermal stress intensity factors for particular cracked FGC strips are presented and discussed. Chapter 6 investigates thermal shock fracture resistance of the edge cracked FGM strips using linear thermal fracture mechanics. Critical thermal shock is introduced; the numerical results for particular FGM strips are provided and interpreted. Chapter 7 gives conclusions for this work.

CHAPTER 2

FRACTURE MECHANICS OF CERAMIC MATERIALS

The brittleness of ceramic materials requires a good understanding of their fracture behavior to prevent catastrophic failures when these materials are used in engineering applications. Ceramics inherently contain flaws and cracks. Under critical loading conditions, these cracks will grow thereby causing material failure. Crack growth occurs when the stress intensity factor reaches a critical value, called fracture toughness K_{Ic}. The study of the stress distribution near a crack tip in a brittle solid is the key to evaluate the stress intensity factor. It is also used to predict what loads or stresses can be safely applied to the ceramic structure and when fracture occurs.

This chapter briefly reviews linear elastic fracture mechanics of ceramics. These theories can be found in fracture mechanics texts (Broek, 1988; Lawn, 1993).

2.1   Basic equations of elasticity

Ceramics can be treated as the ideal elastic material because stress and strain are linearly dependent when a load is applied on a ceramic structure, which means that Hooke's law can be applied. Also, the basic linear elasticity equations are used to evaluate the stress distribution in the near field of the crack tip as shown in Fig. 2.1. In the Cartesian coordinate system, these equations take the following form
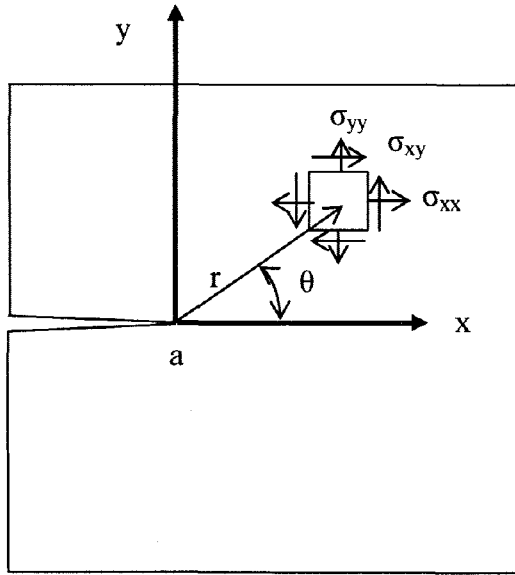
Figure 2.1 Stresses near a crack tip

The equilibrium equations are given by

$$\frac{\partial \sigma_{xx}}{\partial x} + \frac{\partial \sigma_{xy}}{\partial y} = 0,$$

$$\frac{\partial \sigma_{yy}}{\partial y} + \frac{\partial \sigma_{xy}}{\partial x} = 0,$$

(2.1)

where σ_{xx}, σ_{yy}, and σ_{xy} are stresses.

The compatibility equation is

$$\frac{\partial^2 \varepsilon_{xx}}{\partial y^2} + \frac{\partial^2 \varepsilon_{yy}}{\partial x^2} = 2\frac{\partial^2 \varepsilon_{xy}}{\partial x \partial y}.$$

where ε_{xx}, ε_{yy} and ε_{xy} are strains.

(2.2)

10

Hooke's law defines the relations between stress and strain as

$$\varepsilon_{xx} = \frac{1}{E'}(\sigma_{xx} - \nu'\sigma_{yy}),$$

$$\varepsilon_{yy} = \frac{1}{E'}(\sigma_{yy} - \nu'\sigma_{xx}),$$

$$\gamma_{xy} = \frac{1}{2G}\sigma_{xy}.$$

(2.3)

where E is Young's modulus, ν is Poisson's ratio, and $G = \dfrac{E'}{2(1+\nu')}$ is the shear modulus.

For plane strain: $E' = \dfrac{E}{1-\nu^2}$ and $\nu' = \dfrac{\nu}{1-\nu}$. For plane stress: $E' = E$ and $\nu' = \nu$.

Crack tip fields can be conveniently analyzed using polar coordinates. In the polar coordinate system, the basic equations have the following forms

The equilibrium equations

$$\frac{\partial \sigma_{rr}}{\partial r} + \frac{1}{r}\frac{\partial \sigma_{r\theta}}{\partial \theta} + \frac{\sigma_{rr} - \sigma_{\theta\theta}}{r} = 0,$$

$$\frac{1}{r}\frac{\partial \sigma_{\theta\theta}}{\partial \theta} + \frac{\partial \sigma_{r\theta}}{\partial r} + \frac{2\sigma_{r\theta}}{r} = 0,$$

(2.4)

where $r = \sqrt{x^2 + y^2}$, $\theta = \arctan(\dfrac{y}{x})$.

Hooke's law again defines the relation between stresses and strains

$$\varepsilon_{rr} = \frac{1}{E'}(\sigma_{rr} - \nu'\sigma_{\theta\theta}),$$

$$\varepsilon_{\theta\theta} = \frac{1}{E'}(\sigma_{\theta\theta} - \nu'\sigma_{rr}),$$

$$\varepsilon_{r\theta} = \frac{1}{2G}\sigma_{r\theta}.$$

(2.5)

11

2.2   Crack tip stress and displacement

According to linear elastic fracture mechanics, when a ceramic structure with a crack is under a load, there is a stress singularity at the crack tip. That means the stress in region of the crack tip is unbounded. The stress distribution near the crack tip is significant to the strength of the material. There are three modes of fracture, namely, mode I, mode II and mode III, as shown in Fig. 2.2.

| Mode I | Mode II | Mode III |
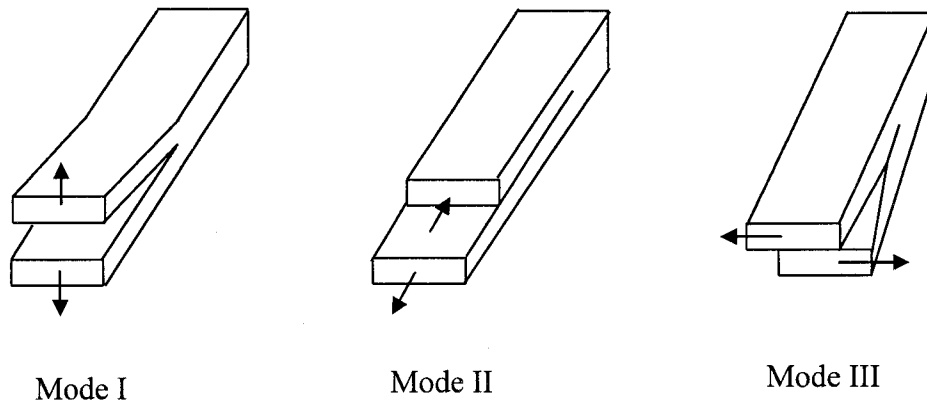
Figure 2.2 Three modes of fracture

Mode I is the opening mode, mode II is the sliding mode and mode III is the tearing mode. Mode I and mode II are in-plane modes and mode III is an out-of-plane mode. Among them, mode I is the most important one for evaluation of fracture resistance because there is always a tendency for a brittle crack to seek an orientation that minimizes the shear loading. In this study, we only consider the mode I crack.

Consider a ceramic structure symmetric about a crack subjected to a mode I load as shown in Fig. 2.3. The crack length is a. Since ceramics are linear elastic materials, we use linear elasticity equations to analyze the stress field near the crack tip.
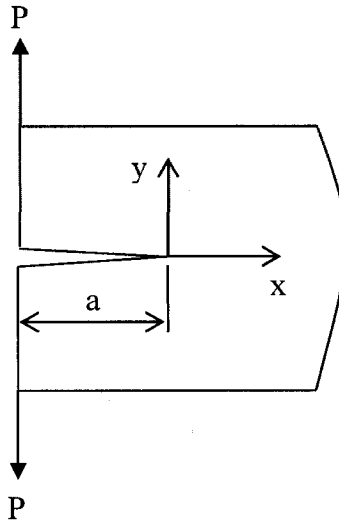
Figure 2.3 A ceramic structure under a mode I load

The boundary conditions of the mode I crack problem come form the facts that there are no tractions on the crack surface and the deformation is symmetric about y = 0.

$$\sigma_{yy} = \sigma_{xy} = 0, \qquad \text{When } y = 0, \quad x < 0.$$

$$v = 0, \qquad\qquad y = 0, \quad x > 0. \qquad\qquad (2.6)$$

$$\sigma_{xy} = 0, \qquad\qquad y = 0, \quad x > 0.$$

Using the basic elasticity equations given in section 2.1, along with the boundary condition of Eq. (2.8), the stress fields of the crack tip are obtained as follows:

13

$$\sigma_{xx} = \frac{K_I}{\sqrt{2\pi r}} \cos\frac{\theta}{2}(1 - \sin\frac{\theta}{2}\sin\frac{3\theta}{2}),$$

$$\sigma_{yy} = \frac{K_I}{\sqrt{2\pi r}} \cos\frac{\theta}{2}(1 + \sin\frac{\theta}{2}\sin\frac{3\theta}{2}), \qquad (2.7)$$

$$\sigma_{xy} = \frac{K_I}{\sqrt{2\pi r}} \sin\frac{\theta}{2}\cos\frac{\theta}{2}\cos\frac{3\theta}{2}.$$

In the polar coordinate system, the stress fields have the following forms (Brian, 1993)

$$\sigma_{rr} = \frac{K_I}{\sqrt{2\pi r}} \cos\frac{\theta}{2}(1 + \sin^2\frac{\theta}{2}),$$

$$\sigma_{\theta\theta} = \frac{K_I}{\sqrt{2\pi r}} \cos^3\frac{\theta}{2}, \qquad (2.8)$$

$$\sigma_{r\theta} = \frac{K_I}{\sqrt{2\pi r}} \sin\frac{\theta}{2}\cos^2\frac{\theta}{2}.$$

After the stress fields are calculated, Hooke's law, along with the following strain displacement relations, can then be used to obtain the displacements of the near crack tip.

$$\varepsilon_{xx} = \frac{\partial u}{\partial x},$$

$$\varepsilon_{yy} = \frac{\partial v}{\partial y}, \qquad (2.9)$$

$$\varepsilon_{xy} = \frac{1}{2}\frac{\partial u}{\partial y} + \frac{\partial v}{\partial x},$$

where u and v denote the horizontal and vertical displacements, respectively. The displacements near the crack tip in the Cartesian coordinate system are given by

$$u = \frac{K_I}{2E}\sqrt{\frac{r}{2\pi}}(1+v)[(2\kappa-1)\cos\frac{\theta}{2} - \cos\frac{3\theta}{2}],$$

$$v = \frac{K_I}{2E}\sqrt{\frac{r}{2\pi}}(1+v)[(2\kappa+1)\sin\frac{\theta}{2} - \sin\frac{3\theta}{2}]. \qquad (2.10)$$

where $\kappa = (3-v)/(1+v)$ for plane stress, and $\kappa = (3-4v)$ for plane strain.

14

2.3 Fracture criterion ($K_I = K_{Ic}$)

In Eq. (2.8), we note that the stresses at the crack tip are singular and the stress intensity is characterized by a parameter K_I. K_I is dependent on the crack geometry and the load. It is called the stress intensity factor (SIF). In general, the stress intensity factor can be evaluated as follows

$$K_I = \beta \sigma \sqrt{\pi a}, \tag{2.11}$$

where a is the crack length for edge crack or half length for interior cracks; σ is the applied stress; and β is a non-dimensional parameter dependent on the crack geometry.

According to equations (2.8) and (2.9), the SIF is the only parameter used to determine the intensity of the stress field near the crack tip. There is a critical value for SIF called the (plane strain) fracture toughness denoted as K_{Ic}. When K_I is smaller than K_{Ic}, the crack does not grow. But, if K_I is equal to K_{Ic}, the crack starts to grow. The fracture criterion in linear elastic fracture mechanics is thus given by

$$K_I = K_{Ic}. \tag{2.12}$$

K_{Ic} indicates the maximum value of stress intensity factor at the crack tip that the material can bear, beyond that, the crack will start to grow. Fracture toughness is a material property; it doesn't vary with a specimen's geometry or load applied.

2.4 Stress intensity factors for typical specimens

SIFs can be obtained using various analytical, numerical, and experimental methods. For typical specimens under typical loads, SIFs can be found in some

handbooks, for example, (Sih, 1973), and Tada et al. (Tada el al., 2000). Here we list the SIF formulas for three typical specimens.

Case I: a uniformly tensile loaded strip with an initial edge crack as shown in Fig. 2.4, the SIF can be calculated using Eq. (2.13). In this case, β is determined by the following equation

$$\beta = 1.12 - 0.231(\tfrac{a}{b}) + 10.55(\tfrac{a}{b})^2 - 21.72(\tfrac{a}{b})^3 + 30.39(\tfrac{a}{b})^4,$$

$$\frac{a}{b} \leq 0.6.$$

(2.13)
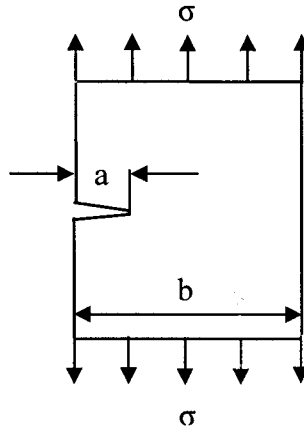
Figure 2.4 Edge cracked strip under a tensile load σ

Case II: an edge cracked strip loaded under a pure bending moment M as shown in Fig. 2.5, the SIF for this case can be obtained by Eq. (2.13). Where β can be determined in the following manner

$$\beta = 1.122 - 1.4(\tfrac{a}{b}) + 7.33(\tfrac{a}{b})^2 - 13.08(\tfrac{a}{b})^3 + 14(\tfrac{a}{b})^4,$$

$$\tfrac{a}{b} \le 0.6.$$

(2.14)

In this case, M is moment per unit thickness, and the stress $\sigma = \dfrac{6M}{b^2}$.

Case III: a three point bending specimen as shown in Fig. 2.6, the SIF can be calculated by Eq. (2.13), where β can be determined by the following equation

$$\beta = 1.106 - 1.552(\tfrac{a}{b}) + 7.71(\tfrac{a}{b})^2 - 13.53(\tfrac{a}{b})^3 + 14.23(\tfrac{a}{b})^4,$$

$$\tfrac{a}{b} \le 0.6.$$

(2.15)

In this case, P is the force per unit thickness, $L = 8b$, and the stress $\sigma = \dfrac{3LP}{2b^2}$.
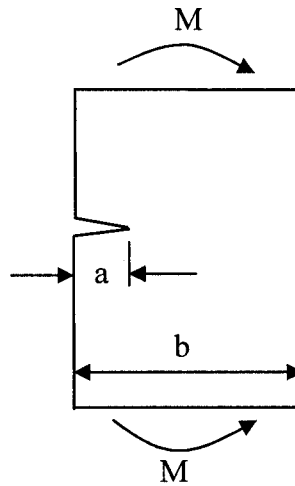
Figure 2.5 Edge cracked strip under a pure bending moment
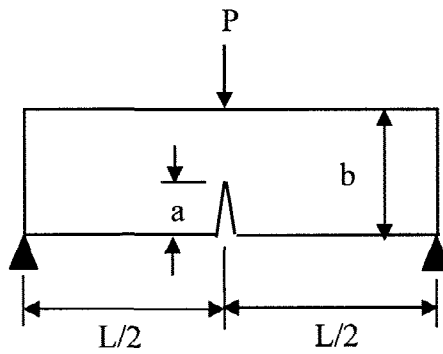
Figure 2.6 Edge cracked strip under a three point bending load

2.5　Fracture toughness for typical ceramic materials

Fracture toughness of ceramic materials is usually much lower than those of metals. In this study, five ceramic materials are involved, i.e., Al_2O_3, Si_3Ni_4, TiC, SiC, and B_4C. The table below lists the fracture toughness and elastic moduli of the typical materials. (Shackelford et al., 1994).

Table 2.1 Fracture toughness and elastic moduli for typical materials

Material	Al_2O_3	Si_3N_4	TiC	SiC	B_4C	Al 1100
Fracture toughness ($MPa\sqrt{m}$)	4.0	5.0	5.0	5.0	4.0	14-28
Young's modulus (*GPa*)	350.0	350.0	450.0	450.0	450.0	69
Poisson's ratio	0.2	0.2	0.2	0.2	0.2	0.33

2.6 Fracture strength

The fracture strength of a cracked ceramic structure can be determined by substituting (2.13) into fracture criterion (2.14), i.e.

$$\beta \sigma_{fr} \sqrt{\pi a} = K_{Ic}. \tag{2.16}$$

which can be rearranged as

$$\sigma_{fr} = \frac{K_{Ic}}{\beta \sqrt{\pi a}}. \tag{2.17}$$

The calculated stress in Eq. (2.19) is called the fracture strength of the ceramic structure. The fracture strength is the strength of a ceramic structure in the presence of a crack. It indicates the maximum stress that could be safely applied on a ceramic structure without causing the pre-existing crack to grow.
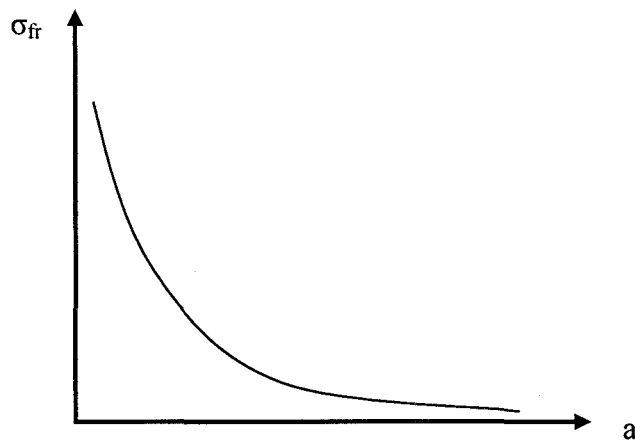
Figure 2.7 Fracture strength vs. crack length

Fig. 2.7 schematically shows that the fracture strength of a ceramic structure depends on the size of the crack length. From the figure, we can see that, for a ceramic structure, the larger the crack length, the lower the fracture strength.

The fracture strength of the typical cases described in section 2.4 can be calculated by the following formulas

For the edge cracked tensile specimen

$$\sigma_{fr} = \frac{K_{Ic}}{(1.12 - 0.231(\frac{a}{b}) + 10.55(\frac{a}{b})^2 - 21.72(\frac{a}{b})^3 + 30.39(\frac{a}{b})^4)\sqrt{\pi a}},$$

$$\frac{a}{b} \leq 0.6.$$

(2.18)

For the edge cracked pure bending specimen

$$\sigma_{fr} = \frac{K_{Ic}}{(1.122 - 1.4(\frac{a}{b}) + 7.33(\frac{a}{b})^2 - 13.08(\frac{a}{b})^3 + 14(\frac{a}{b})^4)\sqrt{\pi a}},$$

$$\frac{a}{b} \leq 0.6.$$

(2.19)

For the three point bending specimen

$$\sigma_{fr} = \frac{K_{Ic}}{(1.106 - 1.552(\frac{a}{b}) + 7.71(\frac{a}{b})^2 - 13.53(\frac{a}{b})^3 + 14.23(\frac{a}{b})^4)\sqrt{\pi a}},$$

$$\frac{a}{b} \leq 0.6.$$

(2.20)

CHAPTER 3

THERMAL STRESSES AND THERMAL SHOCK BEHAVIOR OF CERAMICS

Thermal stress in a ceramic structure is induced by a temperature gradient or an external constraint or the combination of both when the ceramic structure is subjected to a nonuniform thermal load. It can also be induced by the non-homogeneity of the coefficient of thermal expansion within the ceramic structure when a uniform thermal load is applied. In this chapter, basic heat conduction equation, thermoelasticity equations, and the thermal shock behavior of ceramics are reviewed (Boley and Weiner, 1962; Lawn, 1993).

3.1   Basic equations of heat conduction in solids

To determine the thermal stress in an elastic body, we need to have some basic understanding of heat conduction. Conduction heat transfer happens between two particles inside a solid body or two solid bodies with different temperatures that have come in contact.

By Fourier's law, heat conduction inside a solid body is related to the temperature gradient by the following equation

$$q_x = -k \frac{\partial T}{\partial x},$$
$$q_y = -k \frac{\partial T}{\partial y},$$

(3.1)

where q_x and q_y are the heat fluxes, k is the thermal conductivity, and T is the temperature. Here we consider a two-dimensional case. The governing differential equation of heat conduction is

$$\frac{\partial}{\partial x}(k \frac{\partial T}{\partial x}) + \frac{\partial}{\partial y}(k \frac{\partial T}{\partial y}) = \rho c \frac{\partial T}{\partial t},$$

(3.2)

where ρ is the mass density, c is the specific heat, and t is time. For a homogeneous material k, ρ, and c are constants. Eq. (3.2) can be rewritten as

$$\kappa \nabla^2 T = \frac{\partial T}{\partial t},$$

(3.3)

where $\kappa = \frac{k}{\rho c}$ is the thermal diffusivity and the Laplacian of the temperature $\nabla^2 T$ has the following form in the Cartesian coordinate system

$$\nabla^2 T = \frac{\partial^2 T}{\partial x^2} + \frac{\partial^2 T}{\partial y^2}.$$

(3.4)

3.2 Basic equations of thermoelasticity

Generally, ceramics are linear elastic materials. Basic thermoelasticity equations can be employed to solve thermal stress and deformation problems in ceramics. For two-dimensional problems in a rectangular Cartesian coordinate system the equilibrium equations are

$$\frac{\partial \sigma_{xx}}{\partial x} + \frac{\partial \sigma_{xy}}{\partial y} = 0,$$

$$\frac{\partial \sigma_{yy}}{\partial y} + \frac{\partial \sigma_{xy}}{\partial x} = 0.$$

(3.5)

The compatibility equation is

$$\frac{\partial^2 \varepsilon_{xx}}{\partial y^2} + \frac{\partial^2 \varepsilon_{yy}}{\partial x^2} = 2 \frac{\partial^2 \varepsilon_{xy}}{\partial x \partial y}.$$

(3.6)

And, Hooke's law is given by

$$\varepsilon_{xx} = \frac{1}{E'}(\sigma_{xx} - \nu' \sigma_{yy}) + \alpha' \Delta T,$$

$$\varepsilon_{yy} = \frac{1}{E'}(\sigma_{yy} - \nu' \sigma_{xx}) + \alpha' \Delta T,$$

$$\varepsilon_{xy} = \frac{1 + \nu'}{E'} \sigma_{xy}.$$

(3.7)

where $\alpha' = (1 + \nu)\alpha$ for plane strain and $\alpha' = \alpha$ for plane stress. α is the coefficient of thermal expansion and ΔT is the temperature difference between the current and the initial temperature.

3.3 Thermal stress in an infinite strip

A strip is usually used to evaluate the thermal shock fracture resistance of ceramic materials. In this section, thermal stress induced by a thermal shock in an infinitely long strip is reviewed. We assume that the initial temperature of the strip is T_0. Then the temperature on one surface of the strip suddenly drops from T_0 to T_a. The temperature on the opposite surface remains T_0. There is no external mechanical load on the strip, and the body is free from any constraints.

23

3.3.1 Temperature field

In order to solve this thermal stress problem, it is necessary to obtain the temperature field in the infinite strip. The initial conditions for the strip are

$$T = T_0, \qquad t = 0, \qquad 0 \leq x \leq b, \qquad (3.8)$$

And the boundary conditions are

$$
\begin{aligned}
T &= T_a, & x &= 0, & t &> 0, \\
T &= T_0, & x &= b, & t &> 0.
\end{aligned}
\qquad (3.9)
$$

Because there is no applied temperature gradient in the y direction, this is a one-dimensional heat conduction problem, i.e., heat flows only in the x direction as shown in Fig. 3.1
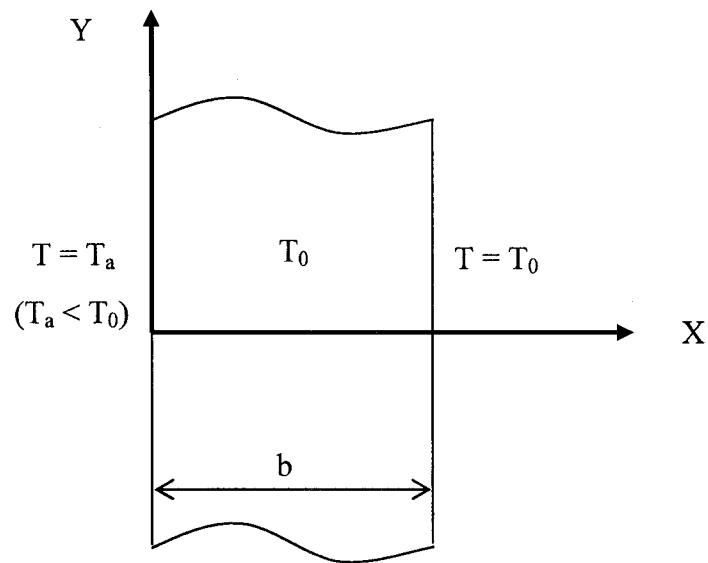
Figure 3.1 Thermal shock on an infinite ceramic strip

24

The temperature in the strip under the initial and boundary conditions as stated in Eq. (3.8) and Eq. (3.9) is given by (Carslaw and Jaeger, 1959; Sucec, 1985)

$$\frac{T-T_0}{T_a-T_0} = 1 - \frac{x}{b} - 2\sum_{n=1}^{\infty}\frac{1}{n\pi}\sin(\frac{n\pi x}{b})e^{-n^2\pi^2\tau},$$

(3.10)

where $\tau = \dfrac{tk}{b^2}$ is the non-dimensional time.

3.3.2 Thermal stress field

After the temperature field is obtained, we can then calculate the thermal stress distribution in the ceramic strip by using the equilibrium equations Eq. (3.5), the compatibility equation Eq. (3.6), and Hooke's law Eq. (3.7) along with the boundary conditions given as

$$\sigma_{xx} = \sigma_{xy} = 0, \qquad x = 0, x = b.$$

(3.11)

Because the temperature is only a function of the coordinate x and the time t, we can assume

$$\begin{aligned}
\sigma_{xx} &= \sigma_{xx}(x,t), \\
\sigma_{xy} &= \sigma_{xy}(x,t), \\
\sigma_{yy} &= \sigma_{yy}(x,t).
\end{aligned}$$

(3.12)

Substituting the above stresses into the equilibrium equation Eq. (3.5) and applying the boundary condition (3.11) leads to

$$\sigma_{xx} = \sigma_{xy} = 0.$$

(3.13)

Then, substituting Eq. (3.13) into Hooke's law Eq. (3.7), the constitutive equations for plain strain become

$$\varepsilon_{xx} = -(1+\nu)(\frac{\nu}{E}\sigma_{yy} - \alpha(T-T_0)),$$

$$\varepsilon_{yy} = \frac{1-\nu^2}{E}\sigma_{yy} + (1+\nu)\alpha(T-T_0), \qquad (3.14)$$

$$\varepsilon_{xy} = 0.$$

Substituting Eq. (3.14) into the compatibility equation Eq. (3.6), gives the governing differential equation for the stress distribution in the infinite strip

$$\frac{\partial^2}{\partial x^2}(\frac{1-\nu^2}{E}\sigma_{yy} + (1+\nu)\alpha(T-T_0)) = 0. \qquad (3.15)$$

After the integration of the above equation with respect to x we have the thermal stress distribution within the strip

$$\frac{1-\nu^2}{E}\sigma_{yy} = -(1+\nu)\alpha(T-T_0) + Ax + B, \qquad (3.16)$$

where, the integration constants A and B can be determined by the conditions of zero resultant force and zero resultant moment on the specimen as follows

$$\int_0^b \sigma_{yy}dx = 0,$$

$$\int_0^b \sigma_{yy}xdx = 0. \qquad (3.17)$$

After finding the two integration constants, A, and B, the following stress distribution is obtained (Jin, 2003)

$$\frac{(1-\nu)\sigma_{yy}}{E\alpha\Delta T} = -2\sum_{n=1}^{\infty}\frac{1}{n\pi}\sin(\frac{n\pi x}{b})e^{-n^2\pi^2\tau} - 4(2-3\frac{x}{b})\sum_{n=1}^{\infty}\frac{(-1)^n-1}{(n\pi)^2}e^{-n^2\pi^2\tau}$$

$$+12(1-2\frac{x}{b})\sum_{n=1}^{\infty}\frac{(-1)^n}{(n\pi)^2}e^{-n^2\pi^2\tau},$$

(3.18)

where $\Delta T = T_0 - T_a$.

3.4 Critical thermal shock ΔT_c

Thermal stress field induced by a temperature gradient is calculated by Eq. (3.18). This stress can be used to evaluate the maximum temperature difference ΔT_c that causes failure of a ceramic strip. It can be proven from Eq. (3.18) that the maximum thermal stress occurs on $x = 0$ immediately after the surface is subjected to the thermal shock. This stress can be calculated by

$$(\sigma_{yy})_{max} = \frac{E\alpha\Delta T}{(1-\nu)}.$$

(3.19)

If we set the maximum thermal stress equal to the tensile strength σ_{TS} of the ceramic material, i.e.

$$(\sigma_{yy})_{max} = \sigma_{TS},$$

(3.20)

the maximum temperature difference that the specimen could bear can be obtained by substituting Eq. (3.19) into Eq. (3.20)

$$\Delta T_c = \frac{(1-\nu)\sigma_{TS}}{E\alpha},$$

(3.21)

where ΔT_c is usually called the critical thermal shock (Lawn, 1993). When $\Delta T < \Delta T_c$, the ceramic strip doesn't fracture and keeps its mechanical integrity.

CHAPTER 4

THERMOELASTICITY OF FUNCTIONALLY GRADED

CERAMICS

In general, functionally graded ceramics (FGCs) are ceramic-ceramic composites. The difference between FGCs and macroscopically homogeneous ceramic-ceramic composites is that FGCs have gradually changed microstructure and material properties. Hence, material properties of an FGC are dependent on spatial position. These material properties may be approximately evaluated by the micromechanics models for conventional composites. To evaluate the thermal shock resistant behavior of FGCs, the related heat conduction and thermoelasticity equations are reviewed and summarized. The effective thermal and elastic material properties of FGC are also reviewed in this chapter.

4.1 Heat conduction equations

FGC composites can be treated as nonhomogeneous materials and their material properties can be approximately evaluated from the conventional micromechanics models for macroscopically homogeneous composites (Reiter et al., 1997; Jin, 2003). In this study, it is assumed that FGCs are graded only in the thickness direction (x direction). In two-dimensional cases, the temperature gradients are related to the heat fluxes in a Cartesian coordinate system by Fourier's law

$$q_x = -k(x)\frac{\partial T}{\partial x},$$

$$q_y = -k(x)\frac{\partial T}{\partial y},$$

(4.1)

where T is temperature, q_x and q_y are the heat fluxes, k(x) is the space-dependent thermal conductivity. The governing differential equation of heat conduction is derived using energy conservation and Fourier's law as follows

$$\frac{\partial}{\partial x}[k(x)\frac{\partial T}{\partial x}] + \frac{\partial}{\partial y}[k(x)\frac{\partial T}{\partial y}] = \rho(x)c(x)\frac{\partial T}{\partial t},$$

(4.2)

where $\rho(x)$ is the space-dependent mass density, c(x) is the space-dependent specific heat, and t is time.

The initial and boundary conditions are needed as follows for solving the differential equation Eq. (4.2):

The initial condition is

$$T = f(x,y), \qquad\qquad t = 0,$$

(4.3)

where $f(x,y)$ is the known temperature at $t = 0$.

The boundary conditions are

$$T = \bar{T}(p,t), \qquad\qquad t \geq 0,$$

(4.4)

Or

$$k(x)\frac{\partial T}{\partial \bar{n}} = -\bar{q}(p,t), \qquad t \geq 0,$$

(4.5)

where p is an arbitrary location on the surface of an FGC body, $\bar{n}$ is the outward normal to the boundary, $\bar{T}$ is the given temperature, and $\bar{q}$ is the given heat flux. The

29

boundary condition Eq. (4.4) gives surface temperature profile, and the boundary condition Eq. (4.5) specifies the heat flux.

4.2 Thermoelasticity equations

Since most FGCs are linearly elastic, the basic thermo-elasticity equations are applicable to FGC specimens. In a Cartesian coordinate system for two-dimensional problems, the elasticity equilibrium equations Eq. (3.5), and the compatibility equation Eq. (3.6) have the same forms. The only difference is Hooke's law because of the spatial variation of material properties

$$
\varepsilon_{xx} = \frac{1}{E(x)'}[\sigma_{xx} - \nu(x)'\sigma_{yy}] + \alpha(x)'\Delta T,
$$

$$
\varepsilon_{yy} = \frac{1}{E(x)'}[\sigma_{yy} - \nu(x)'\sigma_{xx}] + \alpha(x)'\Delta T, \tag{4.6}
$$

$$
\varepsilon_{xy} = \frac{1 + \nu(x)'}{E(x)'}\sigma_{xy},
$$

where for the plain strain

$$
E(x)' = \frac{E(x)}{1 - \nu(x)^2},
$$

$$
\nu(x)' = \frac{\nu(x)}{1 - \nu(x)}, \tag{4.7}
$$

$$
\alpha(x)' = [1 + \nu(x)]\alpha(x),
$$

and for plane strss

$$
E(x)' = E(x),
$$
$$
\nu(x)' = \nu(x), \tag{4.8}
$$
$$
\alpha(x)' = \alpha(x).
$$

30

In the above equations, Young's Modulus E, Poisson's Ratio v, and the coefficient of thermal expansion α are all functions of the coordinate x.

To solve the thermo-elasticity equations of FGCs, we require boundary conditions. In traction boundary conditions, stresses on the boundary are related to the given tractions $\bar{X}$ and $\bar{Y}$ as follows

$$\bar{X} = l\sigma_{xx} + m\sigma_{xy},$$
$$\bar{Y} = m\sigma_{yy} + l\sigma_{xy},$$

(4.9)

where (l, m) define the outward normal to the boundary.

4.3 Effective thermal and elastic properties

Generally, an FGC composite consists of two or more components with different thermal and elastic properties. In this study, we use the micromechanics models for conventional composites to calculate the properties of FGCs. This approach has been proven reasonable if material gradation is not too steep (Reiter and Dvorak, 1998). According to Hashin (Hashin, 1968) the effective thermal conductivity of a two-phase FGC can be calculated as follows

$$V_1 \frac{k_1 - k}{k_1 + 2k} + V_2 \frac{k_2 - k}{k_2 + 2k} = 0,$$

(4.10)

where subscripts 1 and 2 represent the properties of phase 1 and phase 2, respectively. V is the volume fraction of the components and k is the effective thermal conductivity. Hatta and Taya (Hatta and Taya 1986) gave another estimation of thermal conductivity for multiple phase FGCs.

$$k = k_m - \frac{3V_i(k_m - k_i)}{V_m(k_m - k_i) + 3k_m} k_m,$$ (4.11)

where subscripts i and m represent inclusion and matrix properties, respectively. The mass density of an FGC composite may be evaluated by the rule of mixtures and the specific heat can also be estimated approximately by the rule of mixture.

$$\rho = V_1 \rho_1 + V_2 \rho_2.$$ (4.12)

$$c = V_1 c_1 + V_2 c_2.$$ (4.13)

In a two-phase FGC composite, the coefficient of thermal expansion (CTE) may be estimated from the following equation (Levin, 1967)

$$\alpha = \alpha_2 + \frac{\alpha_1 - \alpha_2}{\frac{1}{K_1} - \frac{1}{K_2}} (\frac{1}{K} - \frac{1}{K_2}),$$ (4.14)

where α_1, α_2 represent the CTEs of phase 1 and phase 2, respectively. K_1, and K_2 are the bulk moduli of the components, and K is the effective bulk modulus of the FGC.

Besides thermal properties, the elastic properties of FGCs can also be calculated using the conventional micromechanics model. According to the Mori and Tanaka model (Mori and Tanaka, 1973), (Weng, 1984), (Benveniste, 1987), the effective shear and bulk moduli can be estimated as follows.

The effective shear modulus is given by

$$\mu = \mu_m + \frac{V_i(\mu_i - \mu_m)}{1 + V_m(\mu_i - \mu_m)/[\mu_m + \frac{\mu_m(9K_m + 8\mu_m)}{6(K_m + 2\mu_m)}]},$$ (4.15)

32

where, μ_i represents the shear modulus of the inclusion, and μ_m represents the shear modulus of the matrix.

The effective bulk modulus is

$$K = K_m + \frac{V_i(K_i - K_m)}{1 + V_m \dfrac{K_i - K_m}{K_m + \dfrac{4}{3}\mu_m}},$$

(4.16)

where K_i represents the bulk modulus of the inclusion and K_m represents the bulk modulus of the matrix.

When the Young's modulus and the Poisson's ratio of the FGCs are the constant, the bulk moduli of the two components equal, by substituting Eq. (4.16) into the following equation

$$\alpha = \lim_{K_1 \to K_2}[\alpha_2 + \frac{\alpha_1 - \alpha_2}{\dfrac{1}{K_1} - \dfrac{1}{K_2}}(\frac{1}{K} - \frac{1}{K_2})],$$

(4.17)

the coefficient of thermal expansion (CTE) α can be estimated as follow

$$\alpha = V_1\alpha_1 + V_2\alpha_2$$

(4.18)

The effective shear modulus and bulk modulus then can be used to calculate the effective Young's modulus and Poisson's ratio of the FGC composite by the following elasticity relations

$$E = \frac{9\mu K}{\mu + 3K}.$$

(4.19)

$$\nu = \frac{3K - 2\mu}{2(\mu + 3K)}.$$

(4.20)

After the elastic and thermal properties of FGC composite are obtained, we can use them to analyze the thermal shock behavior of a FGC strip. Since the FGCs considered in this study have constant Young's modulus and Poisson's ratio, the Eq. (4.19) and Eq. (4.20) are not used.

CHAPTER 5

THERMAL CRACKING IN A STRIP OF FUNCTIONALLY

GRADED CERAMIC

We have mentioned in the previous chapters that ceramics always have some inherent flaws, for example, micro surface cracks. The same applies to FGCs. When subjected to a severe thermal shock, an FGC specimen may fracture due to crack propagation. In linear elastic fracture mechanics, we know that the stress intensity factor (SIF), which is proportional to applied stress, is the driving force for crack growth. Under thermal loads, the driving force for the crack growth is the thermal stress intensity factor (TSIF). A number of practical thermal shock problems of FGC specimens can be treated as edge cracked strips under thermal loads. For example, an FGC cutting tool cooled down by the coolant from a high temperature. In this chapter, thermal cracking in an FGC strip is considered. The temperature field and the thermal stress field in a FGC strip under severe thermal shock are calculated, and the TSIF in the edge cracked FGC strip is also evaluated. Numerical results of the temperature fields, thermal stress fields, and TSIFs for the FGC strips, Al_2O_3/Si_3N_4 and TiC/B_4C, are obtained.
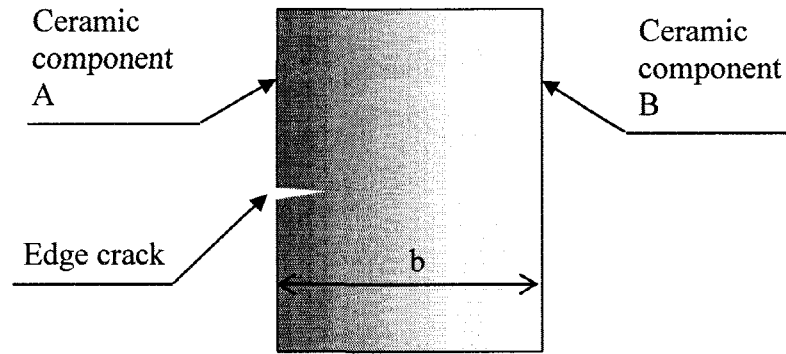
Figure 5.1a An FGC strip with an edge crack

5.1 Temperature

We consider the temperature field of an FGC strip with an edge crack as shown in Fig. 5.1a. The material properties only vary in the thickness direction (x direction). The entire strip is initially at a temperature T_0. Then the temperature of the cracked surface suddenly drops to $T_a < T_0$, and the opposite surface is cooled down to $T_b < T_0$ as shown in Fig. 5.1b. The strip is assumed to be free from external mechanical constraints and loads.
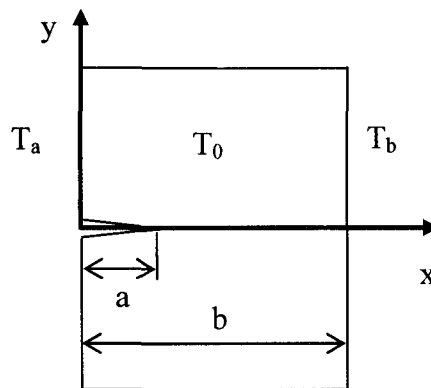
Figure 5.1b An FGC strip subjected to thermal shock

The initial condition of the heat conduction problem is

$$T = T_0, \qquad t = 0, \qquad 0 \le x \le b, \qquad (5.1)$$

where b is the thickness of the FGC strip. The boundary conditions are

$$
\begin{aligned}
T = T_a, & \qquad x = 0, & \qquad t > 0, \\
T = T_b, & \qquad x = b, & \qquad t > 0.
\end{aligned}
\qquad (5.2)
$$

Because initial and boundary temperatures do not vary in the y direction of the strip and the crack does not affect heat flow at short times, the temperature field can be obtained by solving a one dimensional heat conduction problem in the x direction with the following governing differential equation

$$\frac{\partial}{\partial x}(k \frac{\partial T}{\partial x}) = \rho c \frac{\partial T}{\partial t}. \qquad (5.3)$$

Jin (Jin, 2002) obtained a closed-form, short time asymptotic solution of the temperature field in an FGM strip with arbitrary spatial variation of thermal properties using Laplace transforms and their asymptotic properties. The asymptotic temperature field, T(x, τ), has the following form ($\tau \to 0$)

$$
\begin{aligned}
\frac{T(x,\tau)-T_0}{T_0 - T_a} = & -\left[\frac{\rho(0)c(0)k(0)}{\rho(x)c(x)k(x)} \right]^{1/4} erfc\left(\frac{1}{2b\sqrt{\tau}} \int_0^x \sqrt{\frac{\kappa(0)}{\kappa(x)}} dx \right) \\
& -\left(\frac{T_0-T_b}{T_0-T_a} \right)\left[\frac{\rho(b)c(b)k(b)}{\rho(x)c(x)k(x)} \right]^{1/4} erfc\left(\frac{1}{2b\sqrt{\tau}} \int_x^b \sqrt{\frac{\kappa(0)}{\kappa(x)}} dx \right),
\end{aligned}
\qquad (5.4)
$$

where $\tau = t\kappa(0)/b^2$ is the non-dimensional time, $\kappa(x) = k/(\rho c)$ is the thermal diffusivity, $\rho(0)$, $c(0)$, $k(0)$ and $\kappa(0)$ are the values of $\rho(x)$, $c(x)$, $k(x)$ and $\kappa(x)$ at $x = 0$, respectively,

$\rho(b)$, $c(b)$, $k(b)$ and $\kappa(b)$ are the values at $x = b$, respectively, and $erfc( )$ is the complementary error function given by

$$erfc(x) = 1 - \frac{2}{\sqrt{\pi}} \int_0^x \exp(-y^2) dy. \qquad (5.5)$$

The solution given by Eq. (5.4) requires that the FGC strip have continuous and piecewise differentiable thermal properties. Since the thermal stress and TSIF reach their peak values in a very short time when subjected to a thermal shock, the short time temperature solution Eq. (5.4) can be used to evaluate the maximum thermal stress and TSIF (Jin, 2003).

5.2   Thermal stress

The FGC strip considered here is in a plane strain state because the thickness of the strip b is much smaller then its z-dimension.   To obtain the thermal stress, the basic thermal elasticity equations, Eq. (3.5), Eq. (3.6) and the temperature field Eq. (5.4) are used. For plain strain, Hooke's law is as follows

$$\varepsilon_{xx} = \frac{1-\nu^2}{E} (\sigma_{xx} - \frac{\nu}{1-\nu} \sigma_{yy}) + (1+\nu)\alpha(T-T_0),$$

$$\varepsilon_{yy} = \frac{1-\nu^2}{E} (\sigma_{yy} - \frac{\nu}{1-\nu} \sigma_{xx}) + (1+\nu)\alpha(T-T_0), \qquad (5.6)$$

$$\varepsilon_{xy} = \frac{1+\nu}{E} \sigma_{xy}.$$

Here, we only study a special case of a FGC strip having constant Young's modulus and Poisson's ratio. It may narrow the application of the model, but in practice, some FGC composites have this feature, i.e., TiC/SiC, Tic/B_4C, and Al_2O_3/Si_3N_4 FGC systems. The

Young's modulus of each of these FGCs may not change significantly because the constituents have similar Young's moduli.

Since the material properties and the temperature only vary in the x direction of this particular FGC strip, the thermal stresses induced by the temperature gradation are only functions of x and time, as follows

$$
\begin{aligned}
\sigma_{xx} &= \sigma_{xx}(x,t), \\
\sigma_{xy} &= \sigma_{xy}(x,t), \\
\sigma_{yy} &= \sigma_{yy}(x,t).
\end{aligned}
\tag{5.7}
$$

For the traction free surface, the boundary conditions can then be expressed as

$$
\sigma_{xx} = \sigma_{xy} = 0, \qquad \text{at } x = 0, x = b.
\tag{5.8}
$$

Since all the stresses are functions of x, the derivatives of the stresses with respect to y are zeros. Therefore, the equilibrium equation Eq. (3.5) becomes

$$
\begin{aligned}
\frac{\partial \sigma_{xx}}{\partial x} &= 0, \\
\frac{\partial \sigma_{xy}}{\partial x} &= 0,
\end{aligned}
\tag{5.9}
$$

This shows that σ_{xx} and σ_{yy} are both constant. Applying the boundary condition of Eq. (5.8) leads to

$$
\sigma_{xx} = \sigma_{xy} = 0,
\tag{5.10}
$$

Substituting Eq. (5.10) into Hooke's law, Eq. (5.6), we obtain the strains within the strip to be

$$\varepsilon_{xx} = -\frac{(1+\nu)\nu}{E}\sigma_{yy} + (1+\nu)\alpha(x)(T-T_0),$$

$$\varepsilon_{yy} = \frac{1-\nu^2}{E}\sigma_{yy} + (1+\nu)\alpha(x)(T-T_0), \tag{5.11}$$

$$\varepsilon_{xy} = 0.$$

Substituting Eq. (5.11) into the compatibility equation Eq. (3.6) gives the governing differential equation for σ_{yy} of the thermally shocked FGC strip

$$\frac{\partial^2}{\partial x^2}[\frac{1-\nu^2}{E}\sigma_{yy} + (1+\nu)\alpha(x)(T-T_0)] = 0. \tag{5.12}$$

After integration of the partial differential equation Eq. (5.12) we have a general solution of the stress field with two integral constants

$$\frac{1-\nu^2}{E}\sigma_{yy} = -(1+\nu)\alpha(x)(T-T_0) + Rx + S. \tag{5.13}$$

We need two more conditions to determine the integration constants R and S. These two conditions come from the fact that there are no surface forces and moments applied to the strip. The mathematical expressions for these two conditions are

$$\int_0^b \sigma_{yy}dx = 0,$$

$$\int_0^b \sigma_{yy}xdx = 0. \tag{5.14}$$

Applying the conditions Eq. (5.14) into the general solution Eq. (5.13), the two integration constants, R and S, can then be determined. Substituting the constants R an S into Eq. (5.13), the stress distribution in the FGC strip can be obtained as follows

$$\sigma_{yy}^{T}(x,\tau) = -\frac{E\alpha\,\theta(x,\tau)}{1-v} + \frac{E}{(1-v^2)A_0} \times$$

$$\times\left[(A_{22}\text{-}xA_{21})\int_0^b \frac{E\alpha\,\theta(x,\tau)}{1-v}dx - (A_{12}\text{-}xA_{11})\int_0^b \frac{E\alpha\,\theta(x,\tau)}{1-v}xdx\right],$$

(5.15)

where σ_{yy}^{T} is the thermal stress σ_{yy}, $\theta(x,\tau) = T(x,\tau) - T_0$, E is Young's modulus, v is Poisson's ratio, and $\alpha = \alpha(x)$ is the coefficient of thermal expansion. The A_{ij} $(i, j = 1, 2)$ and A_0 are constants and can be found in (Jin, 2003b). They are given by the following equations

$$A_{11} = \frac{Eb}{1-v^2},$$

$$A_{12} = A_{21} = \frac{Eb^2}{2(1-v^2)},$$

$$A_{22} = \frac{Eb^3}{3(1-v^2)},$$

$$A_0 = A_{11}A_{22} - A_{12}A_{21}.$$

(5.16)

5.3 Thermal Stress Intensity Factor

We know that the thermal stress intensity factor (TSIF) is the driving force for crack propagation under thermal load. To obtain TSIF, the basic thermal elasticity equations, i.e., the equilibrium equations, Eq. (3.5); the compatibility equation, Eq. (3.6); and Hooke's law, Eq. (5.6) are solved with given boundary conditions.

Because of the symmetry of the FGC strip, we only consider the upper half of the strip. The mathematical expressions for the boundary conditions of this problem are as follows

$$\sigma_{xx} = \sigma_{xy} = 0, \qquad \text{at } x = 0, x = b, y \geq 0,$$

$$\sigma_{xy} = 0, \qquad \text{at } 0 \leq x \leq b, y = 0,$$

$$\sigma_{yy} = 0, \qquad \text{at } 0 \leq x \leq a, y = 0,$$

$$\text{v} = 0, \qquad \text{at } a \leq x \leq b, y = 0, \tag{5.17}$$

$$\int_0^b \sigma_{yy} dx = 0,$$

$$\int_0^b \sigma_{yy} x dx = 0,$$

To obtain TSIF, several analytical and numerical methods may be used, for example, the finite element method and complex variable method. Here we use the Fourier transform and the singular integral equation method. In this method, stresses have the following expression

$$\sigma_{xx} = \frac{1}{\sqrt{2\pi}} \int_{-\infty}^{\infty} [\zeta^2 (C_1 + D_1 y) e^{-|\zeta|y} - 2D_1 |\zeta| e^{-|\zeta|y}] e^{-ix\zeta} d\zeta$$

$$+ \sqrt{\frac{2}{\pi}} \int_0^{\infty} (-\eta^2)[(A_2 + B_2 x) e^{\eta x} + (C_2 + D_2 x) e^{-\eta x}] \cos(y\eta) d\eta. \tag{5.18}$$

$$\sigma_{yy} = \frac{1}{\sqrt{2\pi}} \int_{-\infty}^{\infty} (-\zeta^2)(C_1 + D_1 y) e^{-|\zeta|y} e^{-ix\zeta} d\zeta$$

$$+ \sqrt{\frac{2}{\pi}} \int_0^{\infty} \{[\eta^2 (A_2 + B_2 x) + 2B_2 \eta] e^{\eta x} \tag{5.19}$$

$$+ [\eta^2 (C_2 + D_2 x) - 2D_2 \eta] e^{-\eta x}\} \cos(y\eta) d\eta.$$

$$\sigma_{xy} = \frac{1}{\sqrt{2\pi}} \int_{-\infty}^{\infty} (i\zeta)[-|\zeta|(C_1 + D_1 y) e^{-|\zeta|y} + D_2 e^{-|\zeta|y}] e^{-ix\zeta} d\zeta$$

$$+ \sqrt{\frac{2}{\pi}} \int_0^{\infty} \eta[\eta(A_2 + B_2 x) e^{\eta x} + B_2 e^{\eta x} \tag{5.20}$$

$$- \eta(C_2 + D_2 x) e^{-\eta x} + D_2 e^{-\eta x}] \sin(y\eta) d\eta.$$

The above stresses satisfy the equilibrium equations and homogeneous compatibility equations. The unknown functions $C_1(\zeta), C_2(\zeta), A_2(\eta),\ B_2(\eta), C_2(\eta)$, and $D_2(\eta)$ can be determined using the boundary conditions Eq. (5.17) and solution Eq. (5.15). Finally, the thermal crack problem can be reduced to the following singular integral equation (Jin, 2003b)

$$\int_{-1}^{1}[\frac{1}{s-r} + K(r,s)]\phi(s,r)ds = -\frac{2\pi(1-\nu^2)}{E}\sigma_{yy}^T(x,\tau), \quad |r| \le 1, \tag{5.21}$$

where $\sigma_{yy}^T(x,\tau)$ is given in Eq. (5.15), and $\phi(r,\tau)$ is the unknown density function defined in following manner

$$\phi(x,\tau) = \frac{\partial v(x,\tau)}{\partial x}, \tag{5.22}$$

where v is the displacement in y direction, $r = 2x/a - 1$. $K(r,s)$ is the kernel as given in Gupta and Erdogan (Gupta and Erdogan, 1974). The function $\phi(r,\tau)$ can also be calculated as (Gupta and Erdogan, 1974)

$$\phi(r,\tau) = \frac{\psi(r,\tau)}{\sqrt{1-r}}, \tag{5.23}$$

where $\psi(r,\tau)$ is continuous for $r \in [-1,1]$. After normalizing the functions $\phi(x,\tau)$ and $\psi(r,\tau)$ by $(1+\nu)\alpha_0 T_0$, the normalized TSIF, K^* at the crack tip can be evaluated as

$$K^* = \frac{(1-\nu)K_I}{E\alpha_0\Delta T\sqrt{\pi b}} = -\frac{1}{2}\sqrt{\frac{a}{b}}\psi(1,\tau), \tag{5.24}$$

43

where K_I represents mode I TSIF, and α_0 is the coefficient of thermal expansion (CTE) at $x = 0$. The details about calculation of the function $\psi(1,\tau)$ can also be found in Gupta and Erdogan (Gupta and Erdogan, 1974).

5.4 Numerical results

The FGCs studied are two phase composites: Al_2O_3/Si_3N_4 and TiC/B_4C. These FGCs can be used in cutting tools because of their high hardness, high temperature and high wear resistance. For example, a Al_2O_3/Si_3N_4 cutting tool can be used to cut steels which can not be cut by Si_3N_4 cutting tools because chemical reactions may occur between the metals and the cutting tools. The volume fractions of the FGC constituents are assumed to follow a power law function. For example, the volume fraction of Si_3N_4 in the Al_2O_3/Si_3N_4 FGC strip is chosen following the power law function Eq. (5.25) and as shown in Fig. 5.2

$$V_{Si_3N_4} = (\frac{x}{b})^p, \qquad (5.25)$$

where p is the power exponent determining the volume fraction of Si_3N_4.
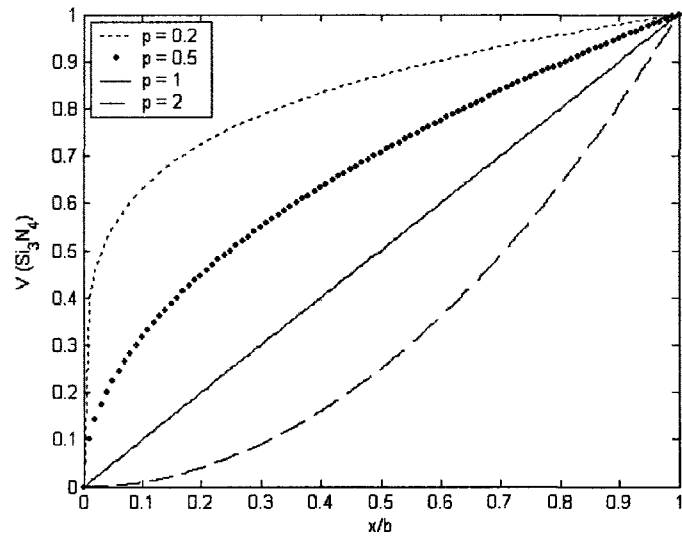
Figure 5.2 Volume fraction of component Si_3N_4 vs. non-dimensional position x/b in an

Al_2O_3/Si_3N_4 FGC strip

Table 5.1 lists the components thermal properties and mass densities of the FGC

strips that were studied (Shackelford et al., 1994).

Table 5.1 Thermal properties and mass densities of FGC components

	Al_2O_3	Si_3N_4	TiC	SiC	B_4C
Coefficient of thermal expansion (CTE) $(10^{-6}/K)$	8.0	3.0	7.0	4.0	4.5
Thermal conductivity (W/m K)	20.0	35.0	20.0	60.0	30.0
Specific heat (kJ/kg K)	0.9	0.7	0.7	1.0	0.95
Mass density (g/cm^3)	3.8	3.2	4.9	3.2	2.5

Fig. 5.3 shows the effective thermal conductivity k of the FGC strip Al_2O_3/Si_3N_4 vs. position x/b calculated by Eq. (4.11). The volume fraction of constituent Si_3N_4 is determined by Eq. (5.25). The three lines represent different power indices, p = 0.2, p = 1, and p = 2, respectively. From this figure we can see that if the power index is less than 1, the effective thermal conductivity of the FGC composite changes rapidly near x/b = 0.
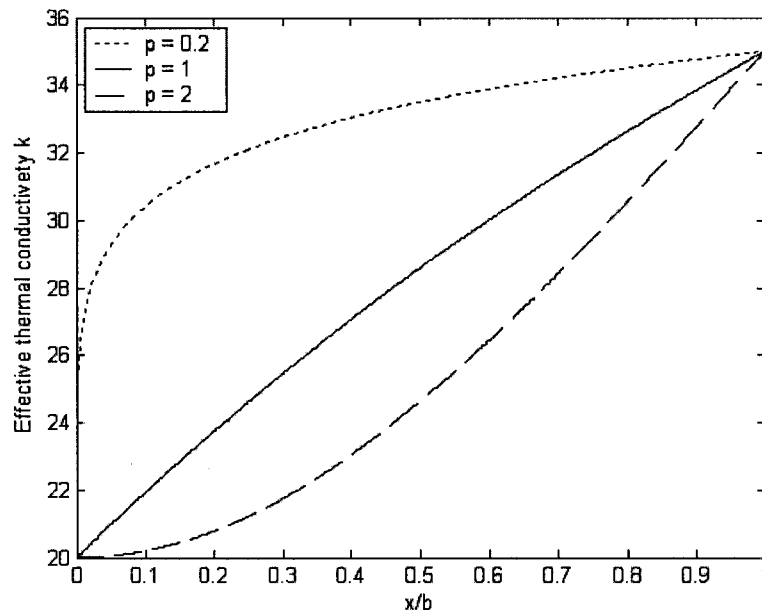
Figure 5.3 Effective thermal conductivity of Al_2O_3/Si_3N_4 FGC strip vs. relative position

x/b for different constituent gradation

In this study, we assume the temperature of the surface opposite the thermally shocked surface is equal to the initial temperature, $T_b = T_0$. Temperatures, thermal stresses and thermal stress intensity factors in the FGC strips are calculated using Eq. (5.4), Eq. (5.15), and Eq. (5.24), respectively. Numerical results are generated by using

FORTRAN code (Jin, 2003b). Similar studies for TiC/SiC FGC were performed in Jin and Paulino (Jin and Paulino, 2001) and Jin (Jin, 2003b).

5.4.1 Temperature

Fig. 5.4 compares the temperature fields of the homogeneous strip calculated by the asymptotic solution used in this study, Eq. (5.4), and the complete solution, Eq. (3.10). The two solutions have good agreement when the non-dimensional time τ is less than 0.1. Since the thermal shock damage occurs shortly after the thermal shock is applied, this model is suitable to evaluate the thermal shock behavior of FGC specimen.
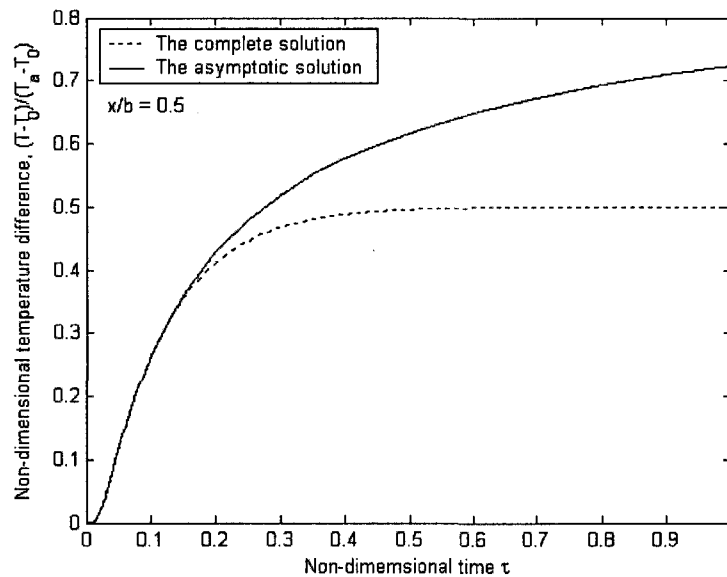

Figure 5.4 The temperature fields for a homogeneous strip calculated with different models
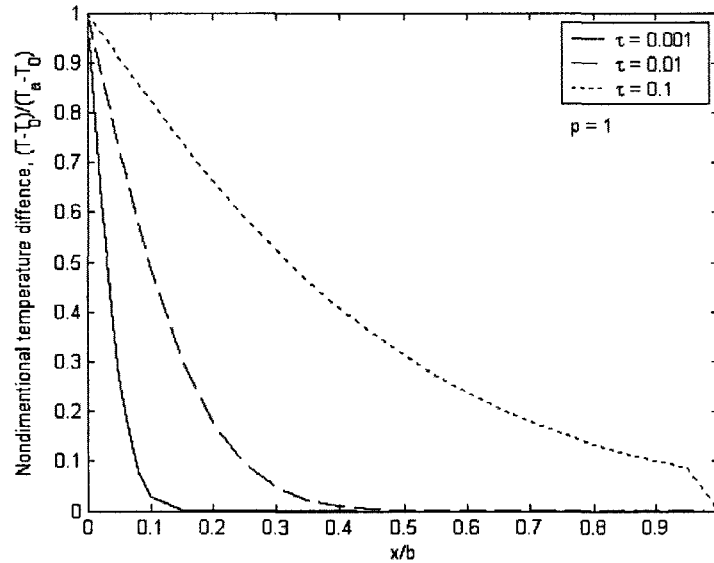
Figure 5.5 Non-dimensional temperature difference vs. non-dimensional position in a

thermally shocked Al_2O_3/Si_3N_4 FGC strip

Fig. 5.5 shows the temperature distribution, $(T - T_0)/(T_a - T_0)$ when a thermal

shock is applied on an Al_2O_3/Si_3N_4 FGC strip. The x axis represents the non-dimensional

position x/b. The y axis indicates the non-dimensional temperature difference. In this

case, the power index p = 1, the three curves represent temperature distributions of the

strip at three instants in time, respectively. From the figure, we can see that the non-

dimensional temperature difference decreases with the increases of the non-dimensional

position, x/b. The non-dimensional temperature difference takes its peak value at x/b=0,

which is at the cracked surface, and the minimum value occurs at x/b=1, which is the

surface opposite the thermally shock. The smaller the value of x/b, the more significant

the change of the non-dimensional temperature difference for the same x/b interval.
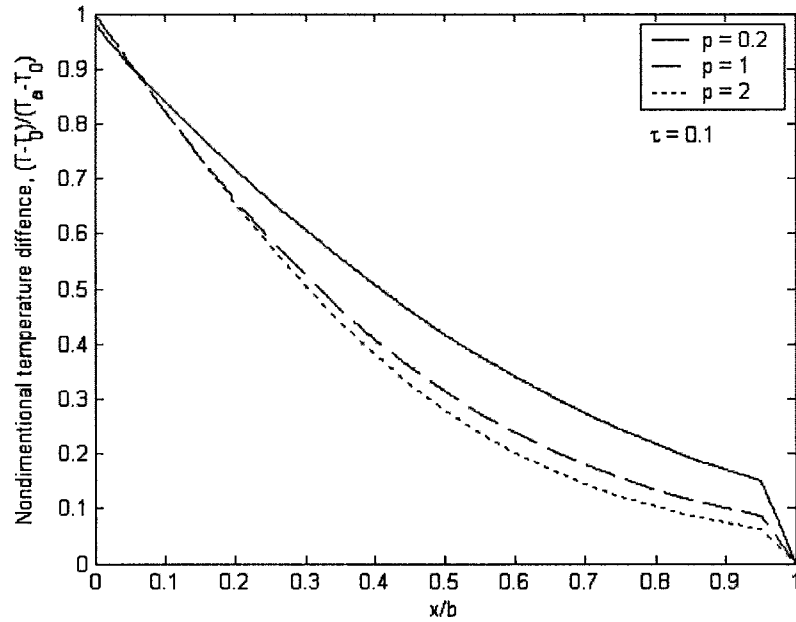
Figure 5.6 Non-dimensional temperature difference vs. non-dimensional position in a

thermally shocked Al_2O_3/Si_3N_4 FGC strip

Fig. 5.6 shows the different behaviors of the temperature distributions for different values of power index p at the same instant of time, $\tau = 0.1$. From the figure we can see that changing the value of p, which means changing the volume fraction of the Si_3N_4, can change the temperature distribution. For example, at the position x/b = 0.5, for p = 0.2, 1, and 2, the non-dimensional temperature differences are 0.42, 0.32, and 0.28, respectively. When x/b = 0, the non-dimensional temperature differences are equal to 1 for all the p values. Fig. 5.6 and Fig. 5.8 couldn't show it clearly because there is a rapid increase for p = 0.2 when x/b is close to zero. Also, there are discontinuities in Fig. 5.6 and Fig. 5.8 for the non-dimensional temperature difference when x/b is close to 1; this is

because of the asympototic nature of the solution. The solution satisfies the boundary condition at x = 1 only approximately and for short time.

Fig. 5.7 and Fig. 5.8 are the numerical results of non-dimensional temperature difference vs. non-dimensional position of x/b for the TiC/B$_4$C FGC strip. Fig. 5.7 shows the non-dimensional temperature difference vs. the non-dimensional position at $p = 1$. Fig. 5.8 gives the non-dimensional temperature difference vs. the non-dimensional position at $\tau = 0.1$. These figures give us similar conclusions in agreement with those from Fig. 5.5, and Fig. 5.6.

Figure 5.7 Non-dimensional temperature difference vs. non-dimensional position in a

thermally shocked TiC/B$_4$C FGC strip

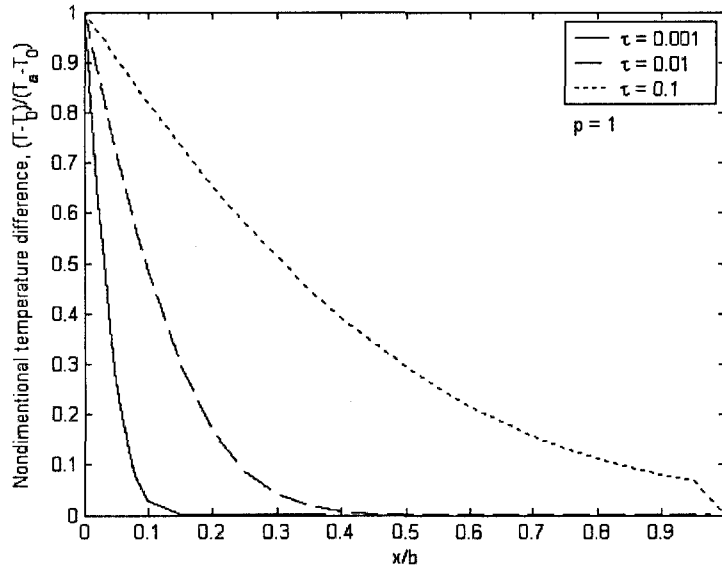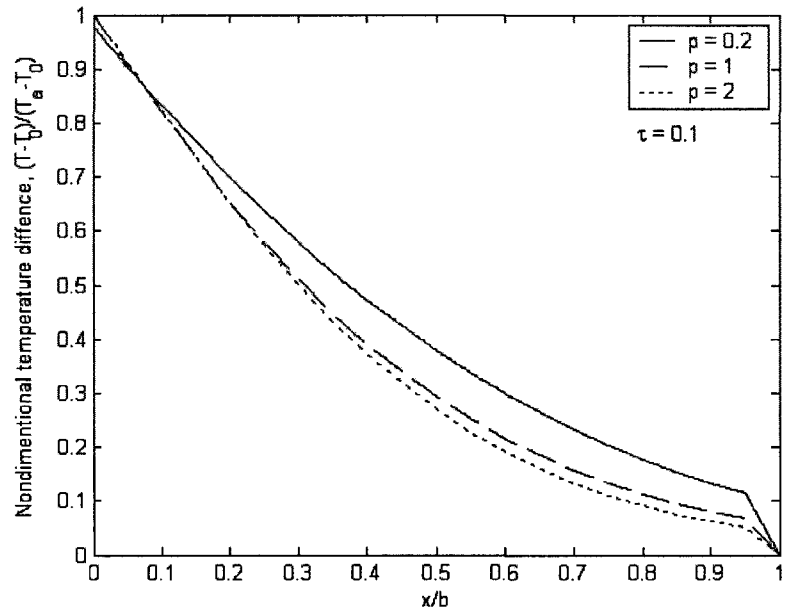*Figure 5.8* Non-dimensional temperature difference vs. non-dimensional position in a

thermally shocked TiC/B$_4$C FGC strip

5.4.2 Thermal stress

Figure 5.9 Non-dimensional thermal stresses vs. non-dimensional positions in a

thermally shocked Al_2O_3/Si_3N_4 FGC strip

Fig. 5.9 shows the non-dimensional thermal stresses $\sigma_{yy}^T(1-v)/E_0\alpha_0(T_0-T_a)$

within the Al_2O_3/Si_3N_4 FGC strip. The horizontal axis indicates the non-dimensional

position x/b in the strip, the vertical axis is the non-dimensional thermal stress caused

by the temperature gradient. The three curves represent three different instants in time.

The power index for this case is p = 0.2. For all time, the maximum thermal stress

occurs at x/b = 0, which is on the thermally shocked surface. For example, at x/b = 0,

the non-dimensional thermal stresses are 0.64, 0.5 and 0.25, for τ = 0.001, 0.01 and 0.1,

respectively. As time increases, the maximum thermal stress decreases first, and then

increases after the minimum value is reached. We also notice from the figure that the

thermal stresses are not always positive. This is because there is no external force and

constraints applied on the thermally shocked FGC strip. Thermal shock brings both

positive and negative stress, so the stresses in the strip can be balanced by themselves.

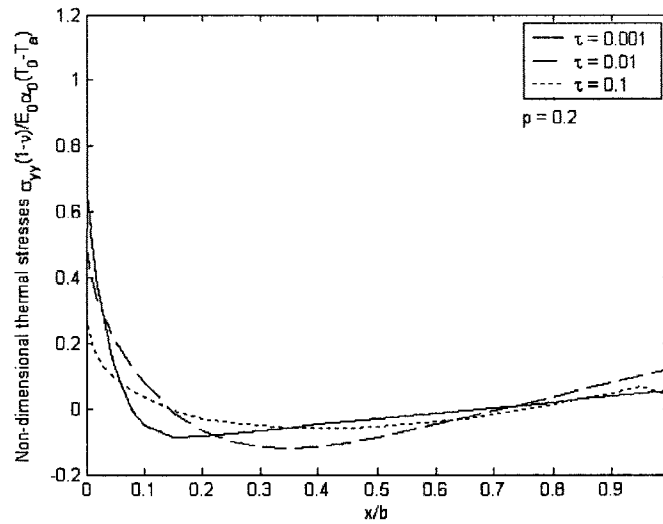*Figure 5.10* Non-dimensional thermal stresses vs. non-dimensional positions in a

thermally shocked Al_2O_3/Si_3N_4 FGC strip

Fig. 5.10 shows similar results as those in Fig. 5.9 but for a different power index.

In this figure, the power index is p = 1. The maximum non-dimensional thermal

stresses for x/b = 0 are 0.8, 0.6, and 0.25 at τ = 0.001, 0.01 and 0.1, respectively.

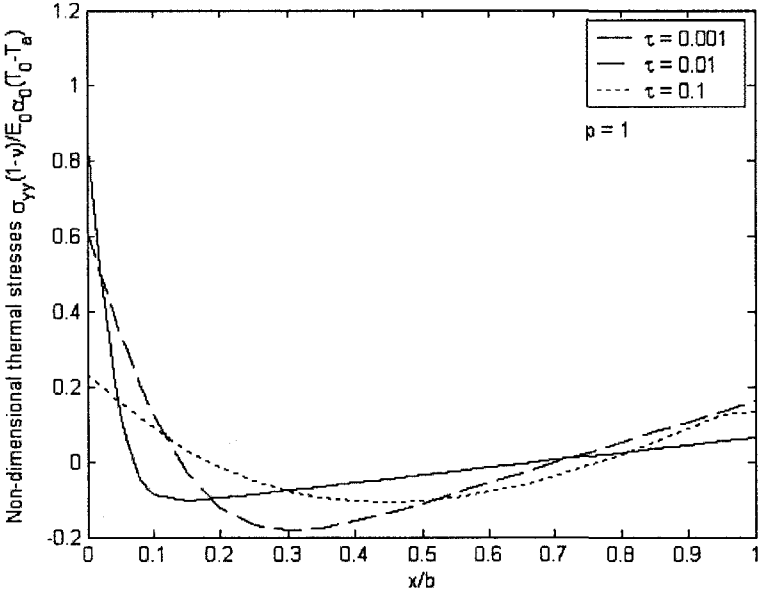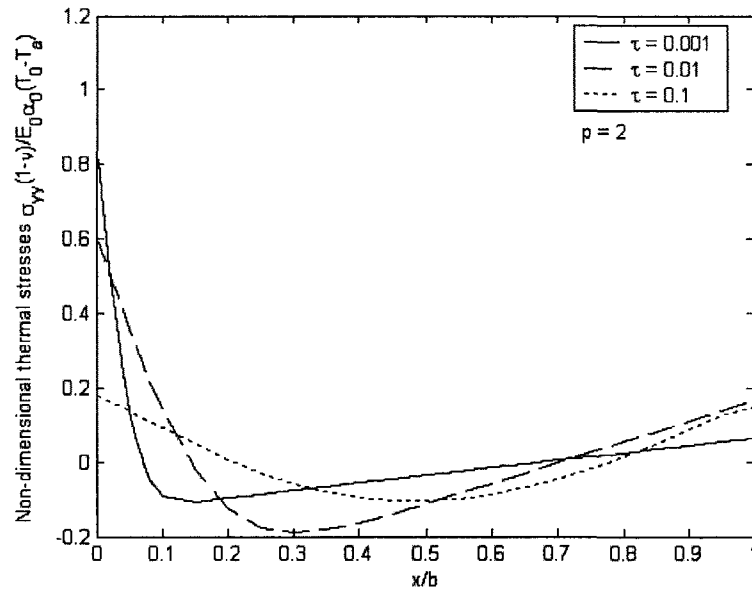*Figure 5.11* Non-dimensional thermal stresses vs. non-dimensional positions in a

thermally shocked Al_2O_3/Si_3N_4 FGC strip

Fig. 5.11 shows similar results as in Fig. 5.9 and Fig. 5.10. In Fig. 5.11, p = 2.

The non-dimensional thermal stresses for x/b = 0 are 0.82, 0.6, and 0.18 at τ = 0.001,

0.01 and 0.1, respectively.
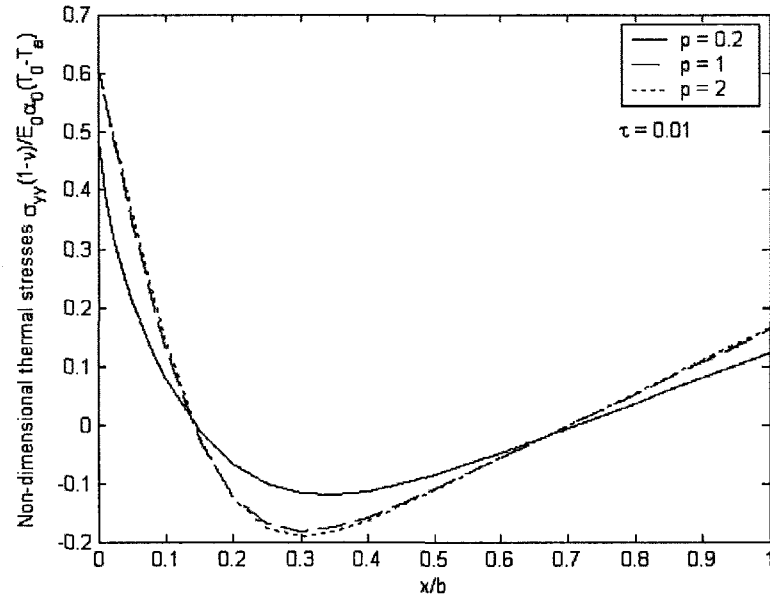
Figure 5.12 Non-dimensional thermal stresses vs. non-dimensional positions for

Al_2O_3/Si_3N_4 FGC strips with different component gradation

Fig. 5.12 shows the thermal stress distributions for different Al_2O_3/Si_3N_4 FGC strips at the same instant of time $\tau = 0.01$. The strips have the power indices p = 0.2, 1, and 2, respectively. In this figure, the horizontal axis is x/b, and the vertical axis is still the non-dimensional thermal stress. It is easy to see the influence of the components' volume fraction on the thermal stress distribution. For example, at x/b = 0, the non-dimensional thermal stress is 0.47 for the FGC strip with the power index p = 0.2 when a thermal shock is applied. But for the FGC strips with p = 1 and 2, the non-dimensional thermal stress is 0.61.

The following figures show the numerical results of the thermal stress distribution for another FGC strip, TiC/B$_4$C, when thermal shocks are applied. Fig. 5.13, Fig. 5.14 and Fig. 5.15 are the non-dimensional thermal stress distributions vs. non-dimensional positions with the same component volume fraction at different instants in time. Fig. 5.13 has the power index $p = 0.2$, and Fig. 5.14 and Fig. 5.15 have the power indices $p = 1$ and $p = 2$, respectively. Fig. 5.16 shows the non-dimensional thermal stress distribution vs. non-dimensional position with different component gradations at time $\tau = 0.01$. These figures support the conclusions we noted from previous figures for Al$_2$O$_3$/Si$_3$N$_4$ FGC strip.

Figure 5.13 Non-dimensional thermal stresses vs. non-dimensional positions in a thermally shocked TiC/B$_4$C FGC strip

Figure 5.14 Non-dimensional thermal stresses vs. non-dimensional positions in a

thermally shocked TiC/B$_4$C FGC strip

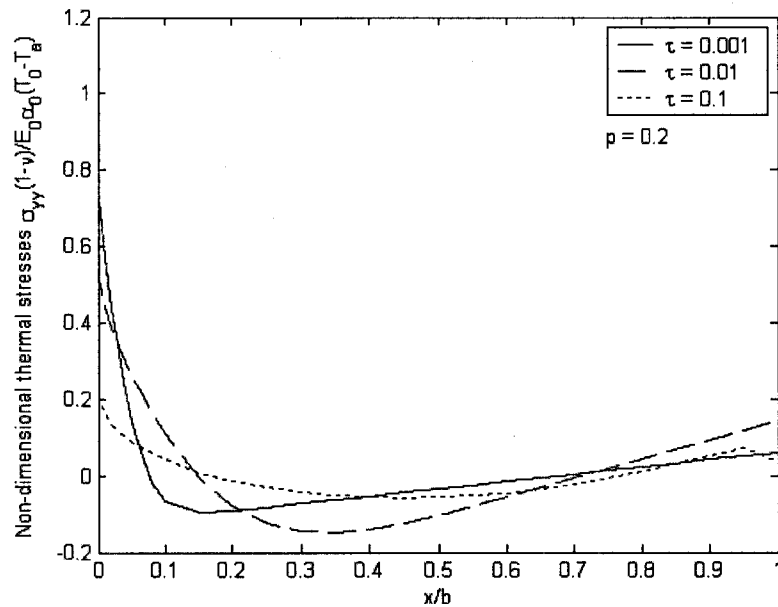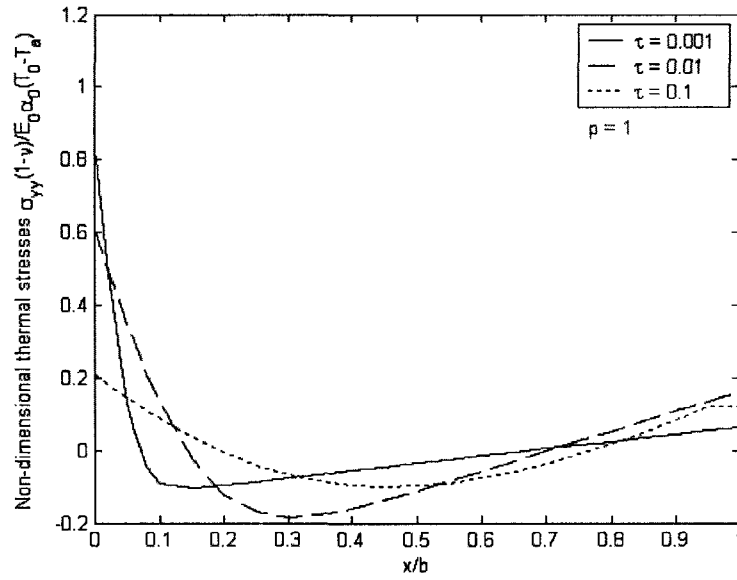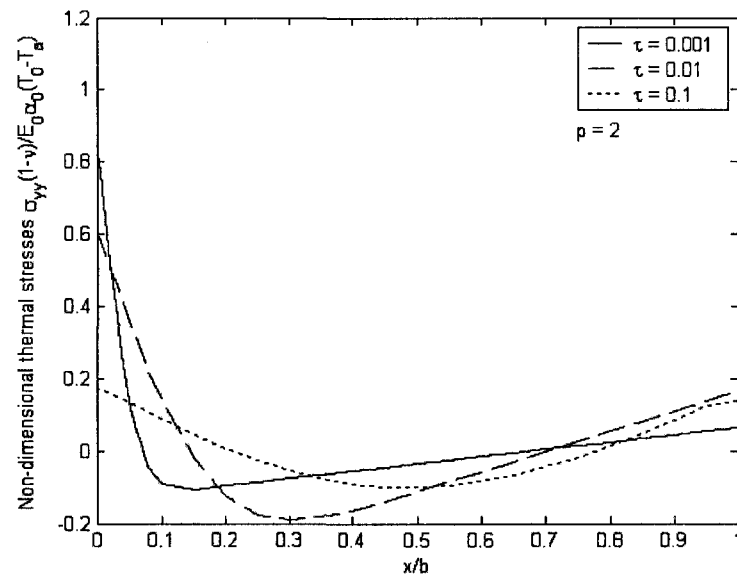*Figure 5.15* Non-dimensional thermal stresses vs. non-dimensional positions in a

thermally shocked TiC/B$_4$C FGC strip

Figure 5.16 Non-dimensional thermal stresses vs. non-dimensional positions for

TiC/B$_4$C FGC strips with different component gradations
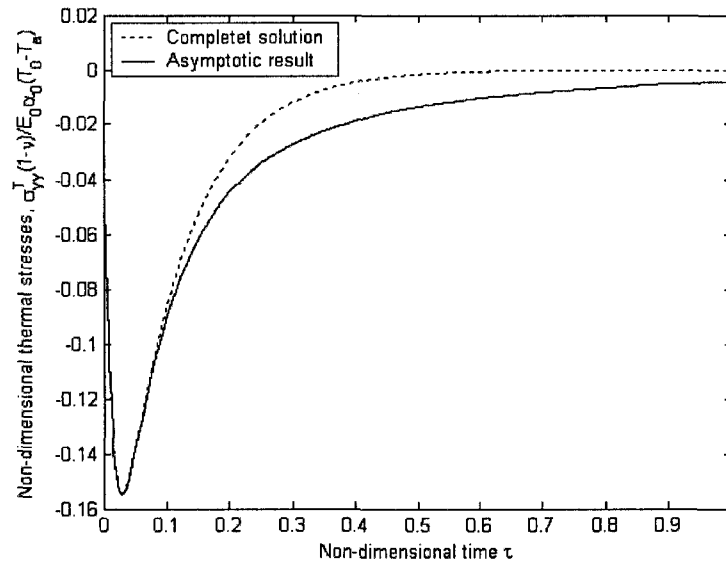
Figure 5.17 Comparison of the asymptotic solution with the complete solution

Fig. 5.17 shows the comparison of the asymptotic solution with the complete solution for the thermal stress distribution in a homogeneous ceramic strip. The vertical axis denotes the non-dimensional thermal stress, the horizontal axis denotes the non-dimensional time. In this figure, the dashed line represents the complete solution and the solid line represents the asymptotic solution. It can be seen that the two solutions agree with each other very well when the non-dimensional time τ is less than 0.1 which means that we can use the numerical model to solve the thermal shock problem because the maximum thermal stress always occurs shortly after the thermal shock is applied.

Fig. 5.18 shows the thermal stresses distributions with the change of non-dimensional time at the thermally shocked surface, x/b=0. The x axis denotes the non-dimensional time $\tau = t\kappa(0)/b^2$ and the y axis denotes the non-dimensional thermal stresses. The three curves represent three different power index values, p = 0.2, p = 1, and p = 2. From this figure we can clearly see that the thermal stresses decrease significantly shortly after the thermal shock is applied. For example, the non-dimensional thermal stresses decrease from 1 to 0.17, 0.22, and 0.33 for p = 2, p = 1, and p = 0.2, respectively, when non-dimensional time changes from 0 to 0.1. Also from the figure; we observe that for the FGC strip with a smaller power index, the thermal stress is larger than the one with the larger power index. For example, at non-dimensional time $\tau = 1$, the non-dimensional thermal stresses are 0.01, 0.06 and 0.25 for p = 2, p = 1, and p = 0.2, respectively.

5.4.3 Thermal stress intensity factor
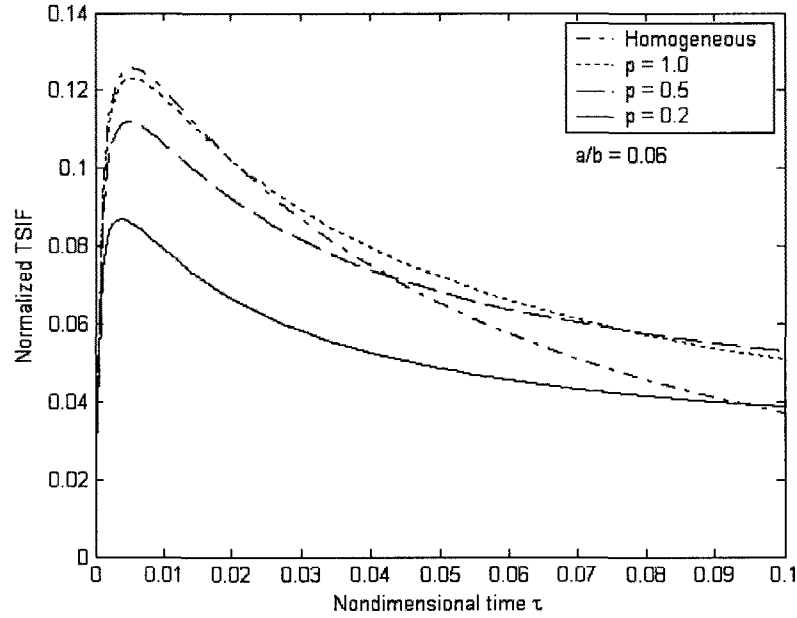
Figure 5.19 Normalized TSIF vs. non-dimensional time for Al_2O_3/Si_3N_4 FGC strips with

different component gradations

Fig. 5.19 shows normalized TSIF vs. non-dimensional time. The x-axis denotes non-dimensional time, the y-axis represents normalized TSIF. In this case, the relative crack length a/b is fixed as 0.06. The figure shows that the maximum TSIF always occurs shortly after the thermal shock is applied, in this case, it is from about $\tau = 0.003$ to $\tau = 0.005$. These maximum values of TSIF are 0.085, 0.112, 0.124, 0.126 for p = 0.2, 0.5, 1.0, and a homogeneous material. The influence of component volume fraction can also be observed from the figure. For example, at time $\tau = 0.01$, the TSIF values are 0.08, 0.107, 0.118, 0.12, for p = 0.2, 0.5, 1.0, and a homogeneous material, respectively.
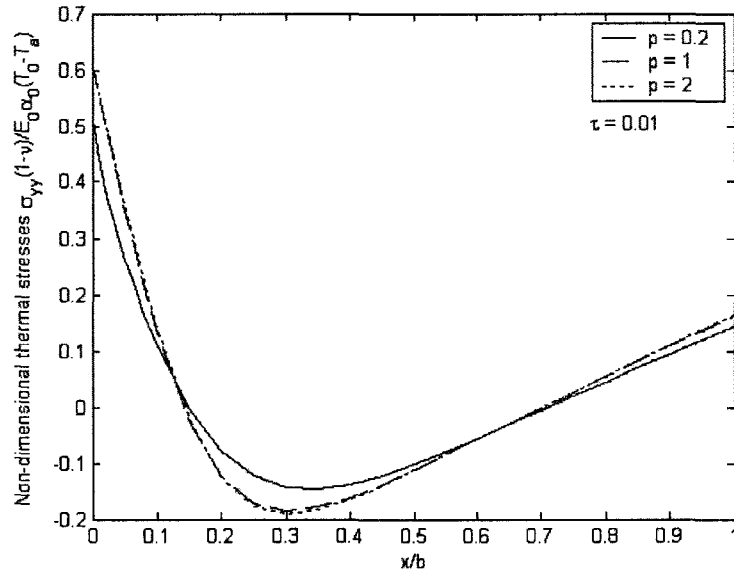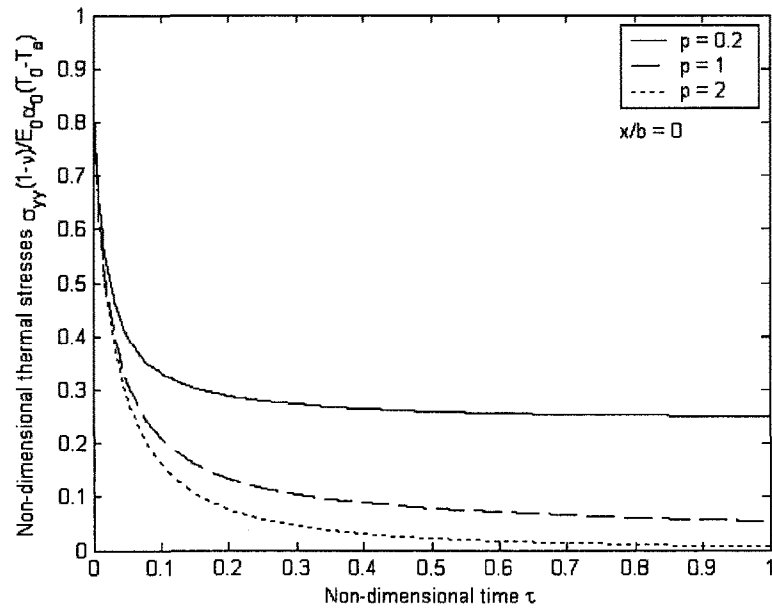
Figure 5.18 Non-dimensional thermal stresses vs. non-dimensional time at x/b = 0 for

TiC/B$_4$C FGC strips with different component gradations
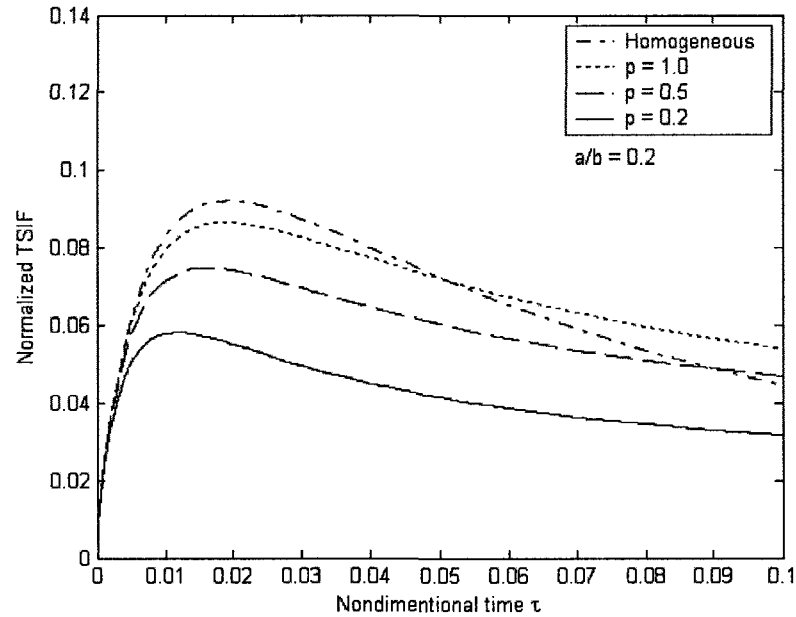
Figure 5.20 Normalized TSIF vs. non-dimensional time for Al_2O_3/Si_3N_4 FGC strips with

different component gradations

Fig. 5.20 shows the normalized TSIF vs. non-dimensional time for relative crack

size a/b = 0.2. The x-axis denotes non-dimensional time, the y-axis represents

normalized TSIF. From this figure we get similar results as those in Fig. 5.19. The

maximum values of TSIF for the crack size a/b = 0.2 are 0.058, 0.075, 0.087, and 0.093,

for power indices p = 0.2, 0.5, 1, and a homogeneous material, respectively. The

maximum values of TSIF in Fig. 5.20 are less than those in Fig. 5.19.
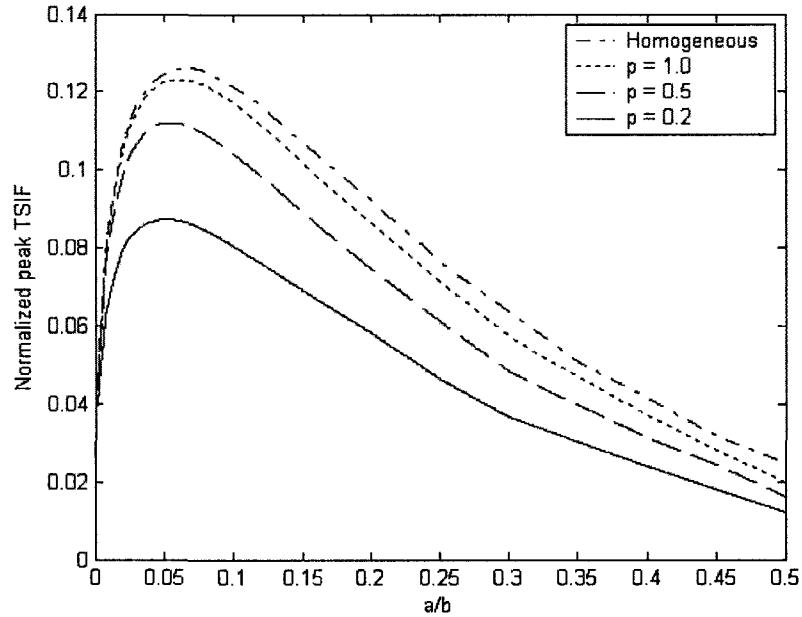
Figure 5.21 Normalized peak TSIF vs. a/b for Al_2O_3/Si_3N_4 FGC strips with different

component gradations

Fig. 21 shows normalized peak TSIF for the FGC strips with different component

volume fractions. The horizontal axis is the relative crack length a/b, the vertical axis is

the normalized peak TSIF. The four curves represent four FGC strips with different

component volume fractions. From the figure, we find that the component volume

fraction has a significant influence on the maximum value of TSIF. For example, the

maximum values of TSIF are 0.088, 0.112, 0.123, and 0.127 for the FGC strips with

power indices p = 0.2, 0.5, 1.0 and the homogeneous material at about a/b = 0.06. We

also observed that the TSIF is related to the crack length. When crack length is smaller

than a certain value, in this figure, it is about a/b=0.06, TSIF increases with increasing

non-dimensional crack length, and reaches its peak value at about a/b=0.06. After the peak value is reached, the value of TSIF decreases with increases in non-dimensional crack length. For example, TSIF = 0.012, 0.016, 0.019, 0.025 for p = 0.2, 0.5, 1.0 and a homogeneous material at a/b = 0.5. In this case, the homogeneous material has the biggest TSIF value.

The following figures show the TSIF for a TiC/B$_4$C FGC strip with different component volume fractions when a severe thermal shock is applied. Fig. 5.22 and Fig. 5.23 show the normalized TSIF distribution vs. non-dimensional time for TiC/B$_4$C FGC strips with different component volume fractions. Fig. 5.22 is for the relative crack size a/b=0.06, and Fig. 5.23 is for a/b=0.2. Fig. 5.24 is the non-dimensional peak TSIF vs. non-dimensional position for the FGC strips with different component volume fractions. From the figures we can conclude similar results as we do from the previous three figures. Here the numerical results are given.
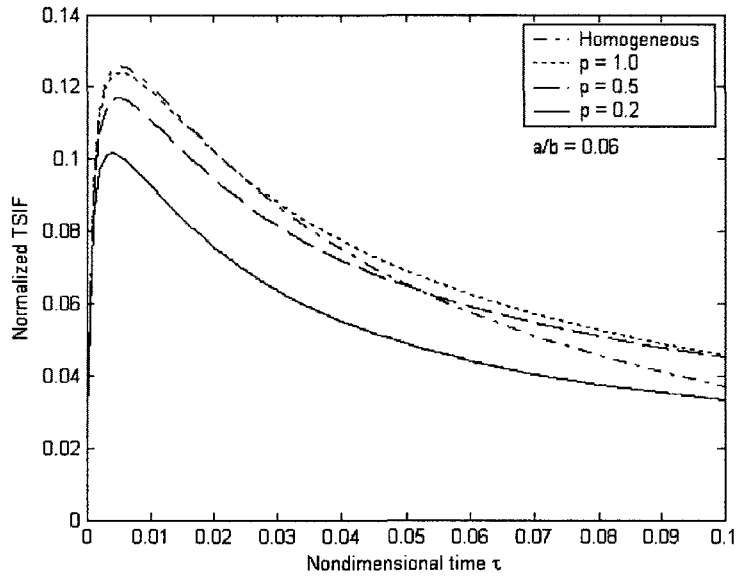
Figure 5.22 Normalized TSIF vs. non-dimensional time for TiC/B₄C FGC strips with

different component gradations
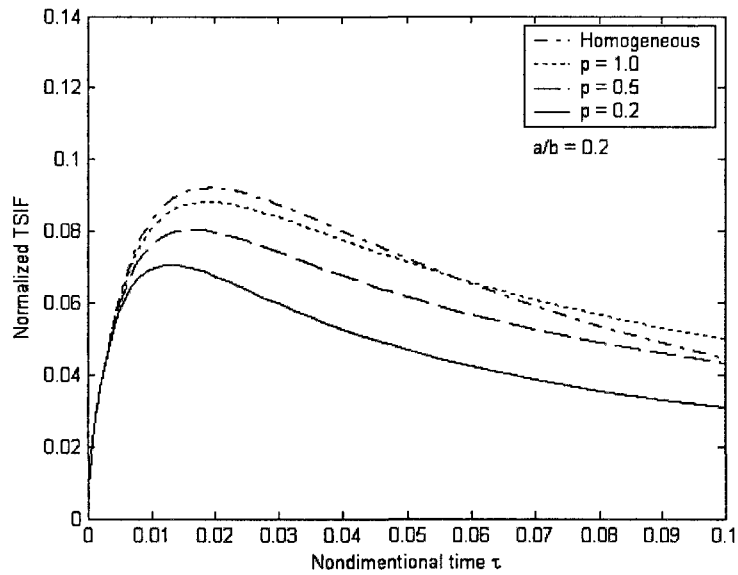
Figure 5.23 Normalized TSIF vs. non-dimensional time for TiC/B₄C FGC strips with

different component gradations
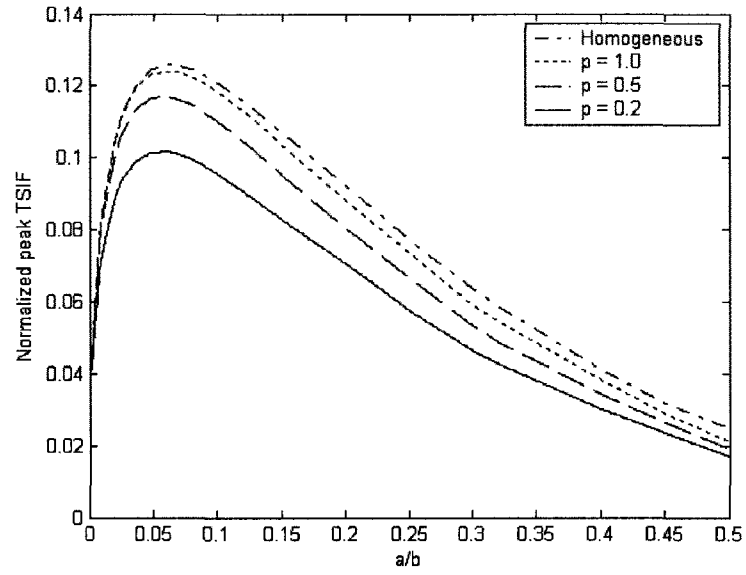
Figure 5.24 Normalized peak TSIF vs. a/b for TiC/B$_4$C FGC strips with different

component gradations

CHAPTER 6

THERMAL FRACTURE RESISTANCE OF A FUNCTIONALLY

GRADED CERAMICS

When thermal shock is applied to a FGC strip, it is critical to know how severe a thermal load can be safely applied. The study of critical thermal shock is the key to predicting the thermal shock behavior of FGCs. The critical thermal shock is the maximum temperature difference applied to an FGC without growing the pre-existing crack when a thermal shock is applied. The critical thermal shock can be obtained by setting TSIF equal to the material toughness and solving for ΔT. The value of ΔT is the critical thermal shock and is denoted by ΔT_c. In this chapter, the critical thermal shock for an FGC is derived along with numerical results for the particular FGC strips, Al_2O_3/Si_3N_4, TiC/SiC and TiC/B_4C.
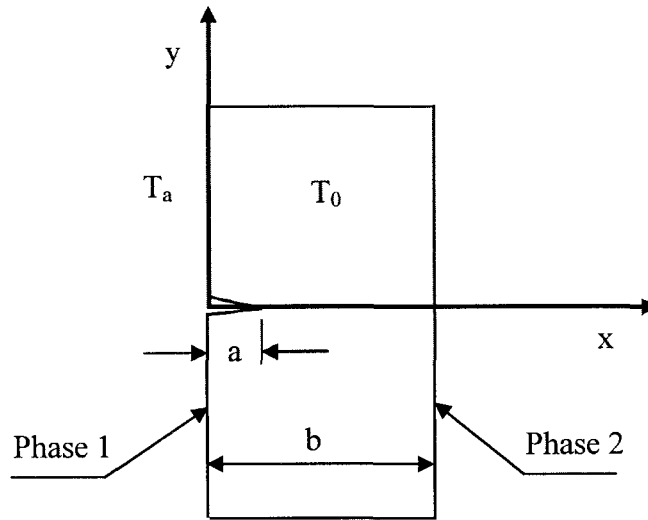
Figure 6.1 An FGC strip with an edge crack under thermal shock

6.1 Critical thermal shock

Fig. 6.1 shows an FGC strip under a thermal shock. We know that the TSIF is related to the severity of the temperature drop on the surface of the FGC strip. The temperature difference on the surface between the initial temperature T_0 and the temperature T_a after the thermal load is applied is the thermal shock

$$\Delta T = T_0 - T_a. \tag{6.1}$$

We also know that TSIF is the driving force for a crack to grow under a thermal shock, and the fracture toughness K_{Ic} is the critical value of TSIF, beyond which the crack will start to propagate. When a thermal load is applied on an FGC strip, there must be a critical value for the thermal shock ΔT at which TSIF is equal to K_{Ic}. This critical

value of thermal shock is the critical thermal shock and is denoted by ΔT_c. It is also known as the thermal shock threshold. When the thermal shock is less than the critical thermal shock, $\Delta T < \Delta T_c$, the crack does not grow, but if $\Delta T \geq \Delta T_c$, the crack starts to propagate. To determine the critical thermal shock, we set the maximum TSIF equal to the fracture toughness K_{Ic}

$$Max_{\{\tau > 0\}}\{K_I(\tau, a, \Delta T_c)\} = K_{Ic}(a), \tag{6.2}$$

where $K_{Ic}(a)$ denotes the fracture toughness of the FGC at $x = a$, and a denotes the pre-existing crack length. Rearranging Eq. (5.24), we obtain TSIF

$$K_I = \frac{E\alpha_0 \Delta T \sqrt{\pi b}}{(1-\nu)}[-\frac{1}{2}\sqrt{\frac{a}{b}}\psi(1, \tau)]. \tag{6.3}$$

Substituting TSIF Eq. (6.3) into Eq. (6.2) yields the critical thermal shock ΔT_c

$$\Delta T_c = \frac{(1-\nu)K_{Ic}(a)}{E\alpha_0 \sqrt{\pi b}} \Big/ Max_{\{\tau > 0\}}\left\{-\frac{1}{2}\sqrt{\frac{a}{b}}\ \psi(1, \tau)\right\}. \tag{6.4}$$

In Eq. (6.4), the fracture toughness of the two-phase FGC composite needs to be determined. The equivalent thermal and elastic property of the FGC composite calculated in chapter 4 does not include the fracture toughness. Here we adopt Jin and Batra's (Jin and Batra, 1996a) rule of mixtures formula for a two phase FGC composite with thermally non-homogeneous but elastically homogeneous properties graded in the x direction.

$$K_{Ic}(x) = \left\{V_1(x)\left(K_{Ic}^1\right)^2 + V_2(x)\left(K_{Ic}^2\right)^2\right\}^{1/2}, \tag{6.5}$$

where $V_i(x)$ ($i = 1, 2$) represents the volume fractions of phase 1 and phase2, respectively. K_{Ic}^1 and K_{Ic}^2 are the fracture toughnesses for phase 1 and phase 2, respectively. The fracture toughnesses of typical ceramic materials can be found in Table 2.1. Substituting the fracture toughness in Eq. (6.5) into Eq. (6.4) gives

$$\Delta T_c = \frac{(1-\nu)\left\{V_1(a)\left(K_{Ic}^1\right)^2 + V_2(a)\left(K_{Ic}^2\right)^2\right\}^{1/2}}{E\alpha_0\sqrt{\pi b}} \bigg/ Max_{\{\tau>0\}}\left\{-\frac{1}{2}\sqrt{\frac{a}{b}}\ \psi(1,\tau)\right\}. \qquad (6.6)$$

6.2   Numerical results

Fig. 6.2 shows the numerical result of the critical thermal shock for the Al_2O_3/Si_3N_4 FGC strips. The two-phase composite is as shown in Fig. 6.1. Phase 1 is Al_2O_3, phase 2 is Si_3N_4, and the thermal shock is applied on the phase 1 Al_2O_3 surface. Two initial crack lengths, $a/b = 0.005$ and $a/b = 0.01$, are considered. The four horizontal lines present the critical thermal shock for the homogeneous materials of phase 1 Al_2O_3 and phase 2 Si_3N_4 with different crack lengths. For example, for the crack length $a/b = 0.005$, the $\Delta T_c = 487.85°K$ for homogeneous Si_3N_4, and $\Delta T_c = 182.95°K$ for homogeneous Al_2O_3, for the crack length $a/b = 0.01$, the $\Delta T_c = 366.53°K$ and $\Delta T_c = 137.45°K$ for homogeneous Si_3N_4, and Al_2O_3 respectively. The volume fraction of phase 2 Si_3N_4 is described by following power law function and is shown in Fig. 5.4.

$$V_2 = (\frac{x}{b})^p, \qquad (6.7)$$

70

From Fig. 6.2 we can see when the power index p is less than 0.5, the critical thermal shock decreases dramatically. For example, at $p = 0.2$, the critical thermal shocks are 222°K and 177°K for $a/b = 0.005$ and $a/b = 0.01$, respectively. At $p = 0.5$, the critical thermal shocks become 189°K and 144°K for the same a/b values. When $p > 0.5$, the critical thermal shocks only decrease slightly. After $p > 1$, the critical thermal shock is almost constant for the two crack lengths. For example, for $a/b = 0.005$ and $a/b = 0.01$, ΔT_c are 183°K and 137°K, respectively. These results tell us that critical thermal shock is changed dramatically by changing the component's volume fraction of the FGC strip when p is less than 1. We can also see from Fig. 6.2 that the critical thermal shock for $a/b = 0.005$ is higher than the critical thermal shock for $a/b = 0.01$, which means increasing the crack length or decreasing the thickness of the strip b can lower the critical thermal shock of the FGC strip.
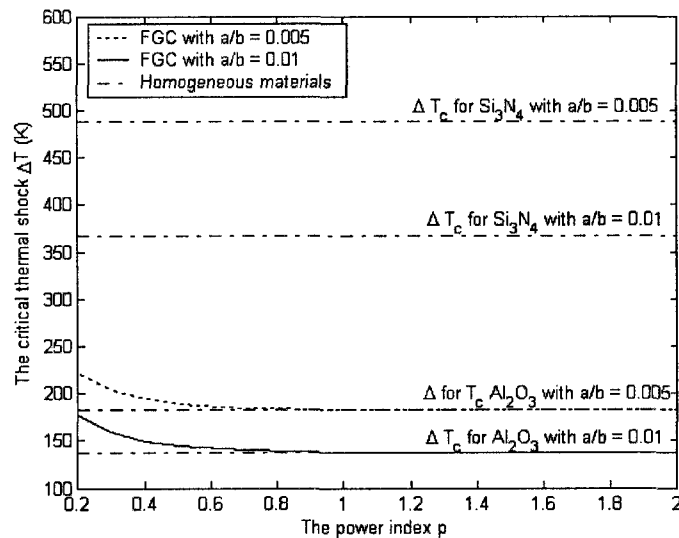
Figure 6.2 Critical thermal shock ΔT_c vs. power index p for Al_2O_3/Si_3N_4 FGC strip

71

Fig. 6.3 gives the numerical results of critical thermal shock for a TiC/SiC FGC strip. In this composite, TiC is phase 1 and SiC is phase 2. The volume fraction of SiC is described by the power law function in Eq. (6.7). The critical thermal shock is applied on the phase 1 TiC surface. Fig. 6.4 gives the numerical results of critical thermal shock for TiC/B$_4$C FGC strip. In this composite, TiC is phase 1 and B$_4$C is phase 2. The volume fraction of B$_4$C is also described by the power law function in Eq. (6.7). The critical thermal shock is applied on the phase 1 TiC surface. We can make similar conclusions from these two figures as we did in Fig. 6.2. For example, when the power index p changes from 0.2 to 0.5, for the crack length $a/b = 0.005$, the critical thermal shocks change from 196°K to 165°K for the TiC/SiC FGC strip, and from 143°K to 130°K for the SiC/B$_4$C FGC strip. Also for the same interval, as p changes from 0.2 to 0.5, for $a/b = 0.01$, the critical thermal shocks change from 155°K to 126°K for TiC/SiC, and from 110°K to 98°K for TiC/B$_4$C.

Comparing the three FGC strips we find that the Al$_2$O$_3$/Si$_3$N$_4$ FGC strip has the highest critical thermal shock, and the TiC/B$_4$C FGC strip has the lowest critical thermal shock. This means that the Al$_2$O$_3$/Si$_3$N$_4$ FGC strip has better thermal shock resistance than the other two FGCs. For example, for the same initial crack length $a/b = 0.005$, and the same power index p = 0.1, the critical thermal shocks are 265°K, 231°K, and 157°K for Al$_2$O$_3$/Si$_3$N$_4$, TiC/SiC, and TiC/B$_4$C FGC strips, respectively.

Figure 6.3 Critical thermal shock ΔT_c vs. power index p for TiC/SiC FGC strip
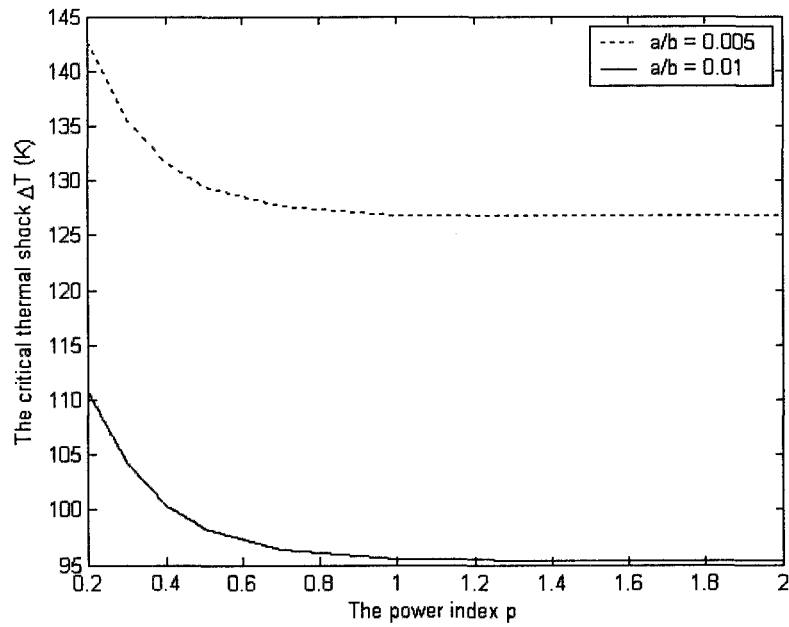
Figure 6.4 Critical thermal shock ΔT_c vs. power index p for TiC/B₄C FGC strip
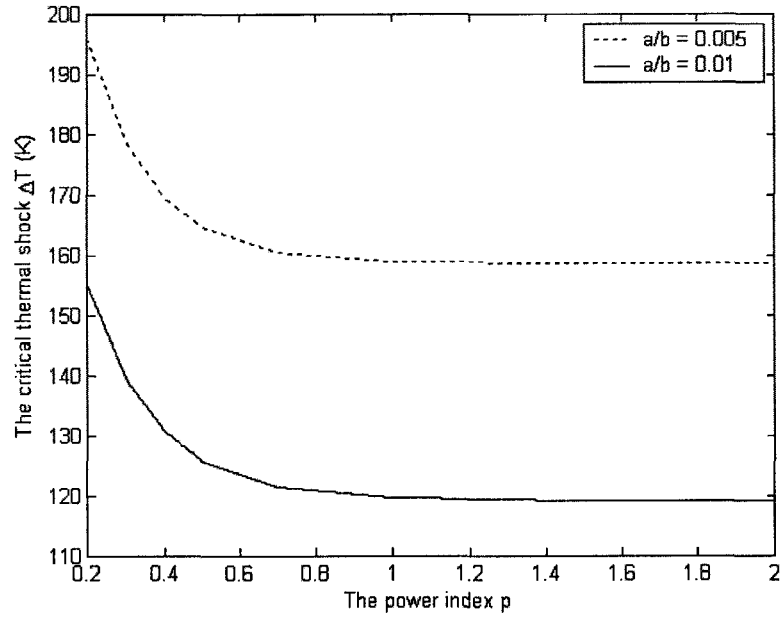
73

CHAPTER 7

CONCLUSIONS

A thermal fracture mechanics approach is used to study the thermal shock fracture behavior of FGC. Three FGC strips Al_2O_3/Si_3N_4, TiC/SiC, and TiC/B_4C, with an initial crack a under a severe thermal shock are considered. The FGC strips are assumed to have constant elastic properties and gradually changing thermal properties in the thickness direction described by a power law function. The temperature field, thermal stress field and thermal stress intensity factor are calculated. The critical thermal shocks for the three FGC strips are obtained. The volume fractions of constituents are critical for the temperature and thermal stress distributions of the thermally shocked FGC strips. Thermal stress intensity factors are dramatically changed when the component gradation is varied. The material gradation profile has a significant influence on the critical thermal shock. The critical thermal shock is increased almost as much as $80^{\circ}K$ for Al_2O_3/Si_3N_4 FGC strip, $70^{\circ}K$ for TiC/SiC FGC strips, and $30^{\circ}K$ for TiC/B_4C FGC strips, when the power index p is changed from 1 to 0.1. For Al_2O_3/Si_3N_4 FGC strip, the result suggests that the bulk of the composite is Si_3N_4 when the thermal shock is applied on the Al_2O_3 surface. Similarly, for the TiC/SiC and TiC/B_4C FGCs, the bulk of the composites are SiC and B_4C when the thermal shocks are applied on the TiC surfaces for both FGC strips. The transition of the component fraction should be rapid and smooth to achieve a higher critical thermal shock value.

REFERENCES

Y. Arai, H. Kobayashi and T. Tamura, 1991, Elastic-plastic thermal stress analysis for optimum design of FGM. *Proc. 4th National Symp. On Functionally Gradient Materials (FGM'91), Functionally Gradient Materials Forum*, Kawasaki, Japan, pp.19-30.

Y. Benveniste, 1987, A new approach to the application of Mori Tanaka's theory in composite materials. *Mechanics of Materials*, 6, 147-157.

B. A. Boley, J. H. Weiner, 1962, *Theory of Thermal Stresses.* John Wiley & Sons, Inc. New York, London.

D. Broek, 1988. *The Practical Use of Fracture Mechanics.* Kluwer Academic Publisher, Dordrecht, Netherlands.

A. Carpinteri and N. Pugno, 2006, Thermal loading in multi-layered and /or functionally graded materials: Residual stress field, delamination, fatigue and related size effects. *International Journal of Solids and Structures*, 43, 828-841.

H. S. Carslaw and J. C. Jaeger, 1959, *Conduction of Heat in Solids.* Clarendon Press, Oxford.

H. J. Choi, T. E. Jin and K. Y. Lee, 1998, Collinear cracks in a layered half-place with a graded nonhomogeneous interfacial zone, Part II: thermal shock response. *International Journal of Fracture*, 94, 123-135.

S. Dag, 2006, Thermal fracture analysis of orthotropic functionally graded materials using an equivalent domain integral approach. *Engineering Fracture Mechanics*, 73, 2802-2828.

S. El-Borgi, L. Hidri and R. Abdelmoula, 2006, An embedded crack in a graded coating bonded to a homogeneous substrate under thermo-mechanical loading. *Journal of Thermal Stresses*, 29, 439-466.

F. Erdogan and B. H. Wu, 1996, Crack problems in FGM layers under thermal stresses. *Journal of Thermal stresses,* 19, 237-265.

T. Fujimoto and N. Node, 2001a, Two crack growth in a functionally graded plate under thermal shock. *Journal of Thermal Stresses*, 24, 847-862.

T. Fujimoto and N. Node, 2001b, Influence of the compositional profile of functionally graded material on the crack path under thermal shock. *Journal of the American Ceramic Society*, 84, 1480-1486.

G. D. Gupta and F. Erdogan, 1974, The problem of edge cracks in an infinite strip. *ASME Journal of Applied Mechanics*, 41, 1001-1006.

Z. Hashin, 1968, Assessment of the self consistent scheme approximation: conductivity of particulate composites. *Journal of Composite Materials*, 2, 284-300.

D. P. H. Hasselman and G. E. Youngblood, 1978, Enhanced thermal stress resistance of structure ceramics with thermal conductivity gradient. *Journal of the American Ceramic Society*, 61, 49-52.

H. Hatta and M. Taya, 1986, Equivalent inclusion method for steady state heat conduction in composites. *International Journal of Engineering Science*, 24, 520-524.

G. Y. Huang, Y. S. Wang and S. W. Yu, 2004, A new model of functionally graded coating with a crack under thermal loading. *Journal of Thermal Stresses*, 27, 491-512.

T. Ishiguro, A. Makino, N. Araki and N. Noda, 1993, Transient temperature response in functionally gradient materials. *International Journal of Thermophysics*, 14, 101-121.

Z.-H. Jin, 2002, An asymptotic solution of temperature field in a strip of a functionally graded material. *International Communications in Heat and Mass Transfer*, 29, 887-895.

Z.-H. Jin, 2003a, Effect of thermal property gradients on the edge cracking in a functionally graded coating. *Surface and Coatings Technology*, 179, 210-214.

Z.-H. Jin, 2003b, Fracture mechanics of functionally graded materials, In: D. Y. Gao and R. W. Ogden, Kluwer (eds), *Advances in Mechanics and Mathematics: Vol. II (AMMA Series, Vol. 4)*, Academic Publishers, Dordrecht, pp. 1-108 (2003).

Z.-H. Jin and R. C. Batra, 1996a, Some basic fracture mechanics concepts in functionally graded materials. *Journal of the Mechanics and Physics of Solids,* 44, 1221-1235.

Z.-H. Jin and R. C. Batra, 1996b, Stress intensity relaxation at the tip of an edge crack in a functionally graded material subjected to a thermal shock. *Journal of thermal stresses,* 19, 317-339.

Z.-H. Jin and N. Noda, 1993, An internal crack parallel to the boundary of a nonhomogeneous half plane under thermal loading. *International Journal of Engineering Science,* 31, 793-806.

Z.-H. Jin and N. Noda, 1994a, Crack-tip singular fields in non-homogeneous materials. *ASME Journal of Applied Mechanics,* 61, 738-740.

Z.-H. Jin and N. Noda, 1994b, An edge crack in a nonhomogeneous half-plane under thermal loading. *Journal of Thermal stresses,* 17, 591-599.

Z.-H. Jin and N. Noda, 1994c, Transient thermal stress intensity factors for a crack in a semi-infinite plane of a functionally gradient material. *International Journal of Solids and Structures,* 31, 203-218.

Z.-H. Jin and G. H. Paulino, 2001, Transient thermal stress analyses of an edge crack in a functionally graded material. *International Journal of Fracture,* 107, 73-98.

A. Kawasaki and R. Watanabe, 1987, Finite element analysis of thermal stress of the metal ceramic multilayer composites with controlled compositional gradients. *Journal of the Japan Institute of Metals,* 51, 525-529.

A. Kawasaki and R. Watanabe, 1993a, Fabrication of disk-shaped functionally gradient materials by hot pressing and their thermo-mechanical performance. In: J.B. Holt, M. Koizumi, T. Hirai, and Z. A. Munir (eds.), *Ceramic transactions, Vol. 34: Functionally Gradient Materials, American ceramic Society,* Westerville, Ohil, pp. 157-164.

A. Kawasaki and R. Watanabe, 1993b, Thermal shock fracture mechanism of metal-ceramic functionally gradient materials. In: G. A. Schneider and G. Petzow (eds), *Thermal Shock and Thermal Fatigue Behaviour of Advanced Ceramics,* Kluwer Academic Publ., Dordrecht, pp. 509-529.

M. Koizumi, 1993, The concept of FGM. In: J. B. Holt, M. Koizumi, T. Hirai and Z. A. Munir (eds.), *Ceramic transactions, Vol. 34: Functionally Gradient materials,* American Ceramic Society, Westerville, Ohio 1993, pp. 3-10.

K. Kokini and S.V. Rangaraj, 2005, Time-dependent behavior and fracture of functionally graded thermal barrier coatings under thermal shock. *Functionally Graded Materials VIII Materials Science Forum,* 492-493, 379-384.

Y. Kuroda, K. Kusaka, S. Moro, and M. Togawa, 1993, Evaluation tests of ZrO_2/Ni functionally gradient materials for regeneratively cooled thrust engine applications. In: J. B. Holt, M. Koizumi, T. Hirar, and Z. A. Munir (eds.), *Ceramic Transactions, Vol. 34: Functionally Graded Materials,* American Ceramic Society, Westerville, Ohio, pp. 289-296.

B. R. Lawn, 1993. *Fracture of Brittle Solid.* Cambridge: Cambridge University Press.

Y. D. Lee and F. Erdogan, 1998, Interface cracking of FGM coatings under steady-state heat flow. *Engineering Fracture Mechanics,* 59, 361-380.

V. M. Levin, 1967, Thermal expansion coefficients of heterogeneous material. *Mekh. Tver. Tela,* 2, 88-94

T. Mori and K Tanaka, 1973, Average stress in matrix and average elastic energy of materials with misfitting inclusions. *Acta Materialia,* 21, 571-574.

M. Nemat-Alla and N. Noda, 2000, Edge crack problem in a semi-infinite FGM plate with a bidirectional coefficient of thermal expansion under two dimensional thermal loading. *Acta Mechanica,* 144, 211-229.

N. Noda, 1997, Thermal stresses intensity factor for functionally gradient plate with an edge crack. *Journal of Thermal Stresses,* 20, 373-387.

N. Noda, 1999, Thermal stresses in functionally graded materials. *Journal of Thermal Stresses,* 22, 477-512.

N. Noda and Z.-H. Jin, 1993, Thermal stress intensity factors for a crack in a strip of a functionally graded material. *International Journal of Solids and structures,* 30, 1039-1056.

N. Noda and T. Tsuji, 1991a, Crack tip singularity fields in nonhomogeneous body under thermal stress fields. *JSME International Journal, Series A,* 38 364-369.

N. Noda and T. Tsuji, 1991b, Steady thermal stresses in a plate of a functionally gradient material with temperature-dependent properties. *Trans. Japan Soc. Mech. Eng.,* A57, 625-631.

Y. Obata and N. Noda, 1993a, Transient thermal stresses in a plate of functionally gradient material. In: J. B. Holt, M. Koizumi, T. Hirai, and Z. A. Munir (eds.), *Ceramic Transactions, Vol. 34: Functionally Gradient Materials,* American Ceramic Society, Westerville, Ohio, pp. 403-410.

Y. Obata and N. Noda, 1993b, Unsteady thermal stresses in a functionally gradient material plate. *Trans. Japan Soc. Mech. Eng.,* A59, 1090-1103.

M.-J. Pindera, J. Aboudi, and S. M. Arnold, 2002, Analysis of spallation mechanism in thermal barrier coatings with graded bond coats using the higher-order theory of FGMs. *Engineering Fracture Mechanics,* 69, 1587-1606.

L. F. Qian, R. C. Batra, 2005, Three dimensional transient heat conduction in a functionally graded thick plate with a higher-order plate theory and a meshless local Petro-Galerkin method. *Computational Mechanics,* 35, 214-226.

S. Rangaraj and K. Kokini, 2004, A study of thermal fracture in functionally graded thermal barrier coatings using a cohesive zone model. *Journal of Engineering Materials and Technology-Transactions of the ASME,* 126, 103-115.

T. Reiter and G. J. Dvorak, 1998, Micromechanical models for graded composite materials. *Journal of the Mechanics and Physics of Solids,* 46, 1655-1673.

T. Reiter, G. J. Dvorak, and V. Tvergaard, 1997, Micromechanical models for graded composite materials. *Journal of the Mechanics and Physics of Solids,* 45, 1281-1302.

F. S. Pettit and G. W. Goward, *Coatings for High Temperature Applications.* In: E. Lang (ed.), Applied Science Publishers, London, p. 341.

K. Satyamurthy, D. P. H. Hasselman, J. P. Singh, and M. P. Kamat, 1990, Effect of spatial variation of thermal conductivity on magnitude of tensile thermal stresses

in brittle materials subjected to convective heating. In: D. P. Hasselman and R. A. Heller (eds.), *Thermal Stresses in Severe Environments*, Plenum Press, New York, pp. 325-342.

J. F. Shackelford, W. Alexander, and J. S. Park, 1994, *CRC Materials Science and Engineering Handbook.* CRC Press, Inc, Boca Raton, Florida.

G. C. Sih, 1973, *Handbook of Stress Intensity Factors.* Institute of fracture and solid mechanics, Lehigh University, Bethlehem, Pennsylvania.

J. Sucec, 1985. *Heat Transfer*, Wm. C. Brown Publishers, Dubuque, Iowa.

H. Takahashi, T. Ishikawa, D. Okugawa, and T. Hashida, 1993, Laser and plasma-ARC thermal shock/fatigue fracture evaluation procedure for functionally gradient materials. In G. A. Schneider and G. Petzow (eds), *Thermal Shock and Thermal Fatigue Behaviour of Advanced Ceramics,* Kluwer Academic Publ., Dordrecht, pp 543-554.

H. Tada, P. C. Paris, and G. R. Irwin, 2000, *The Stress Analysis of Cracks Handbook.* ASME press, New York.

Y. Tanigawa, 1995, Some basic thermoelastic problems for nonhomogeneous materials. *ASME Applied Mechanics Review*, 48, 287-300.

Y. Tanigawa, T. Akai, R. Kawamura, and N. Oka, 1996, Transient heat conduction and thermal stress problems of a nonhomogeneous plate with temperature-dependent material properties. *Journal of Thermal Stresses,* 19, 77-102.

Y. Tanigawa, T. Muraki, and R. Kawamura, 1996, Evaluation of axisymmetric steady thermal stress and thermal stress intensity factor in Kassier's nonhomogeneous infinite body with a penny-shaped crack. *JSME International Journal, Series A*, 39, 540-547.

S. Ueda, 2001, Thermal shock fracture in a W-Cu divertor plate with a functionally graded nonhomogeneous interface. *Journal of Thermal Stresses*, 24, 1021-1041.

S. Ueda, 2002, Transient thermal singular stresses of multiple cracking in a W-Cu functionally graded divertor plate. *Journal of Thermal Stresses*, 25, 83-95.

S. S. Vel and R. C. Batra, 2002, Exact solution for thermoelastic deformations of functionally graded thick rectangular plates. *American Institute of Aeronautics and Astronautics Journal*, 40, 1421-1433.

S. S. Vel and R. C. Batra, 2003, Three-dimensional analysis of transient thermal stresses in functionally graded plates. *International Journal of Solids and Structures*, 40, 7181-7196.

B. L. Wang, J. C. Han, and S. Y. Du, 2000, Thermoelastic fracture mechanics for nonhomogeneous material subjected to unsteady thermal load. *ASME Journal of Applied Mechanics*, 67, 87-95.

B. L. Wang, Y. W. Mai, and X. H. Zhang, 2004, Thermal shock resistance of functionally graded materials. *Acta Materialia*, 52, 4961-4872.

G. J. Weng, 1984, Some elastic properties of reinforced solids with special reference to isotropic ones containing spherical inclusions. *International Journal of Engineering Science*, 22, 845-856.

B. Yildirim, S. Dag and E. Erdogan, 2005, Three dimensional fracture analysis of FGM coatings under thermomechanical loading. *International Journal of Fracture*, 132, 369-395.

J. Zhao, X. Ai, J. X. Deng, and J. H. Wang, 2004, Thermal shock behaviors of functionally graded ceramic tool materials. *Journal of the European Ceramic Society*, 24, 847-854.

J. Zhao, X. Ai, and X. P. Huang, 2002, Relationship between the thermal shock behavior and the cutting performance of a functionally gradient ceramic tool. *Journal of Materials Processing Technology*, 129, 161-166.

BIOGRAPHY OF THE AUTHOR

Wenjin Luo was born in Beijing, China. He studied in Beijing Union University from 1982 to 1987 and graduated with a Bachelor's degree in Chemical Engineering. He worked as processing engineer in Beijing Oxygen Plant from 1987 to 1990. He then worked as a research and development engineer in Beijing Specialty Gases Institute and other industrial companies for more than 10 years. He came to The University of Maine to pursue a Master of Science degree in Mechanical Engineering in January 2004. He joined the Mechanical Engineering graduate program as a teaching assistant and research assistant.

Luo is a candidate for the Master of Science degree in Mechanical Engineering from The University of Maine in December, 2006.